The Zonal Seasonal Cycle of Tropical Precipitation: Introducing the Indo-Pacific Monsoonal Mode

P. J. TUCKMAN,[a] JANE SMYTH,[a] NICHOLAS J. LUTSKO,[b] AND JOHN MARSHALL[a]

[a] *Department of Earth, Atmospheric, and Planetary Sciences, Massachusetts Institute of Technology, Cambridge, Massachusetts*
[b] *Scripps Institution of Oceanography, San Diego, California*

(Manuscript received 6 March 2023, in final form 20 March 2024, accepted 1 April 2024)

ABSTRACT: The intertropical convergence zone (ITCZ) is associated with a zonal band of strong precipitation that migrates meridionally over the seasonal cycle. Tropical precipitation also migrates zonally, such as from the South Asian monsoon in Northern Hemisphere summer (JJA) to the precipitation maximum of the west Pacific in Northern Hemisphere winter (DJF). To explore this zonal movement in the Indo-Pacific sector, we analyze the seasonal cycle of tropical precipitation using a 2D energetic framework and study idealized atmosphere–ocean simulations with and without ocean dynamics. In the observed seasonal cycle, an atmospheric energy and precipitation anomaly forms over South Asia in northern spring and summer due to heating over land. It is then advected eastward into the west Pacific in northern autumn and remains there due to interactions with the Pacific cold tongue and equatorial easterlies. We interpret this phenomenon as a "monsoonal mode," a zonally propagating moist energy anomaly of continental and seasonal scale. To understand the behavior of the monsoonal mode, we develop and explore an analytical model in which the monsoonal mode is advected by low-level winds, is sustained by interaction with the ocean, and decays due to the free tropospheric mixing of energy.

SIGNIFICANCE STATEMENT: Regional concentrations of tropical precipitation, such as the South Asian monsoon, provide water to billions of people. These features have strong seasonal cycles that have typically been framed in terms of meridional shifts of precipitation following the sun's movement. Here, we study zonal shifts of tropical precipitation over the seasonal cycle in observations and idealized simulations. We find that land–ocean contrasts trigger a monsoon with concentrated precipitation over Asia in northern summer and near-surface eastward winds carry this precipitation into the west Pacific during northern autumn in what we call a "monsoonal mode." This concentrated precipitation remains over the west Pacific during northern winter, as further migration is impeded by the cold sea surface temperatures (SSTs) and easterly winds of the east Pacific.

KEYWORDS: Intertropical convergence zone; Tropics; Atmospheric circulation; Energy transport; Hadley circulation; Walker circulation

1. Introduction

The seasonal cycle is one of the most striking aspects of the climate system. Over the course of the year, peak solar insolation moves between the southern and northern ends of the tropics, dominating the variability of global climate. One of the many important manifestations of the seasonal cycle is the meridional movement of the intertropical convergence zone (ITCZ), associated with a band of strong precipitation that stretches zonally around most of Earth. The ITCZ is connected with the ascending branch of the Hadley circulation, which exports energy from the hemisphere where the ITCZ is located. This observation has led to an "energetic" framework for understanding the meridional position of the zonal-mean ITCZ. In this framework, the ITCZ moves toward the warmer hemisphere (Broccoli et al. 2006; Privé and Plumb 2007b; Kang et al. 2008; Donohoe et al. 2013), enabling that hemisphere to cool via cross-equatorial atmospheric energy transport. Similarly, the ITCZ can be thought of as being collocated with the energy flux equator (EFE)—the latitude at which the meridional energy flux is zero and its derivative with respect to latitude is positive (Bischoff and Schneider 2016; Adam et al. 2016b; Wei and Bordoni 2018). The energetic framework also rationalizes how the ocean damps meridional ITCZ shifts on interannual time scales by contributing to energy transport away from the warmed hemisphere (Green and Marshall 2017; Green et al. 2017, 2019; Luongo et al. 2022).

While the seasonal cycle of solar forcing is zonally symmetric, Earth's continental configuration and ocean heat transport are not, leading to strong zonal asymmetries in the distribution of tropical rainfall and the ITCZ. For example, the South Asian monsoon can be viewed as a local amplification of ITCZ precipitation (Privé and Plumb 2007a; Biasutti et al. 2018), and there is more precipitation in the tropical west Pacific (~130°–190°E) during northern winter than at other times of the year or elsewhere at similar latitudes. This seasonal cycle of Indo-Pacific precipitation has been viewed as the migration of a single convective system steered by the diagonal configuration of Asia, the Maritime Continent, and Australia (Heddinghaus and Krueger 1981; Meehl 1987, 1993; Chang et al. 2005).

Denotes content that is immediately available upon publication as open access.

Corresponding author: P. J. Tuckman, ptuckman@mit.edu

DOI: 10.1175/JCLI-D-23-0125.1

The energetic framework has been applied to zonally asymmetric precipitation by calculating the EFE in zonal sectors or as a function of longitude (e.g., Privé and Plumb 2007a; Schneider et al. 2014; Shaw et al. 2015; Bischoff and Schneider 2016; Adam et al. 2016a; Zhou and Xie 2018; Lutsko et al. 2019; Atwood et al. 2020; Mamalakis et al. 2021), a method that traditionally ignores zonal energy transport and associated zonal overturning circulations (Zhai and Boos 2015). An alternative approach, introduced in Boos and Korty (2016), uses an "energy flux potential" (χ; defined in section 2a) to represent atmospheric energy transport. The energy flux potential (EFP) can be thought of as a 2D extension of the EFE: Just as the EFE is the location of zero meridional energy transport, the EFP maximum is the location of zero zonal and meridional energy transport. Boos and Korty (2016) showed that enhanced precipitation follows the maximum of the EFP on seasonal or longer time scales and large spatial scales, both being located over South Asia in northern summer (JJA) and over the equatorial west Pacific in northern winter (DJF).

In this work, we build on Boos and Korty (2016) by providing a detailed description of the observed seasonal cycle of the EFP and associated precipitation. To study the underlying mechanisms, we run simulations with an idealized coupled atmosphere–ocean general circulation model (GCM), using a shallow slab ocean to represent Asia and thin barriers to represent the other continents. Using this model, we identify and introduce the "monsoonal mode," an energy and precipitation anomaly that forms over Asia in summer and is advected eastward while being sustained by interactions with the surface.

Our paper is organized as follows. Section 2 describes the EFP and its seasonal cycle as seen in reanalysis data. Section 3 presents simulated seasonal cycles of precipitation and the EFP in a simplified coupled GCM and compares simulations with reanalysis. The general concept of a monsoonal mode and an idealized model of it are introduced in section 4, and the role of the ocean in preventing the monsoonal mode from propagating into the east Pacific is discussed in section 5. Finally, section 6 summarizes our findings, discusses their implications, and proposes areas of future research.

2. The seasonal cycle of energy transport and precipitation in reanalysis data

a. Computation of the energy flux potential

Precipitation occurs where there is ascending air, which generally leads to energy export via high-altitude divergent winds exporting dry static energy. Therefore, net energy export can be used to predict the location and intensity of tropical precipitation (Neelin and Held 1987). The connection between energetics and precipitation in the meridional direction is mediated by the Hadley circulation, which exports energy from the tropics through high-altitude winds and causes heavy precipitation in its ascending branch. This framework can also be applied zonally, as vertical motion leads to both energy export and precipitation, regardless of the direction in which the energy is exported. We therefore use the EFP, χ, defined such that its gradients are the divergent component of atmospheric energy transport to predict meridional and zonal structures of precipitation simultaneously. The relationship between the EFP and precipitation is complicated by factors such as small-scale topography and variations in gross moist stability, but precipitation broadly follows EFP maxima, i.e., locations from which the atmosphere is exporting energy, on large spatial scales and long time scales. Additionally, the EFP can predict how forcings will affect precipitation, while other variables used for studying tropical precipitation, such as subcloud entropy, are purely diagnostic.

The EFP is defined such that its Laplacian is the 2D divergence ($\boldsymbol{\nabla}\cdot$) of the vertically integrated horizontal transport of moist static energy $\langle \mathbf{u}\mathrm{MSE}\rangle$, so the rotational component of energy transport is removed (Boos and Korty 2016):

$$\nabla^2\chi = -\boldsymbol{\nabla}\cdot\langle \mathbf{u}\mathrm{MSE}\rangle, \tag{1}$$

with ∇^2 being the horizontal 2D Laplacian acting on the scalar EFP and MSE being

$$\mathrm{MSE} = Lq + gz + c_pT, \tag{2}$$

where q is the specific humidity, z is the height, T is the temperature, and the constants $L \equiv 2.25 \times 10^6$ J kg^{-1}, $g \equiv 9.8$ m s^{-2}, and $c_p \equiv 1005$ J kg^{-1} K^{-1} are the latent heat of vaporization of water, the acceleration due to gravity, and the specific heat of air at constant pressure, respectively. A negative sign is included in Eq. (1) so that energy is fluxed from high to low values of EFP.

To calculate the EFP in reanalysis, we use the monthly mass-corrected divergence of total energy (Mayer et al. 2022) from the ERA5 (Hersbach et al. 2020). The calculated divergence includes a component from kinetic energy though this contribution is very small compared to the MSE defined above (e.g., compare a kinetic energy of 50 J kg^{-1} for wind moving at 10 m s^{-1} to an MSE difference of 10^4 J kg^{-1} for a 10-K difference in air temperature). All data are averaged from 1979 to 2020 to calculate climatological means.

The annual mean atmospheric EFP is shown in Fig. 1. Energy is transported poleward from the tropics, but there is also substantial zonal structure, with increased energy export from the west Pacific and the Maritime Continent, as well as from northeastern South America and the tropical west Atlantic.

b. The seasonal cycle

Figure 2 shows the seasonal cycle of the EFP and precipitation, with precipitation smoothed spatially by a simple moving mean. The meridional positions of the EFP maximum and precipitation roughly follow the solar forcing over the course of the year, but their zonal structures are more complicated. In April (top left panel), the EFP is mostly zonally symmetric, with small maxima in the west Pacific and near South America ($\leq$0.1 PW, compared with meridional differences of 2 PW). The position of the EFP maximum in April shows substantial interannual variability, appearing anywhere from the mid-Atlantic to sub-Saharan Africa to the southwest Pacific (not shown). In May, there is a pronounced maximum over the Asian sector, focused over India (~0.3 PW), which is robust from year to year. Over the course of northern summer (JJA), this EFP peak intensifies and moves slightly northeast. This

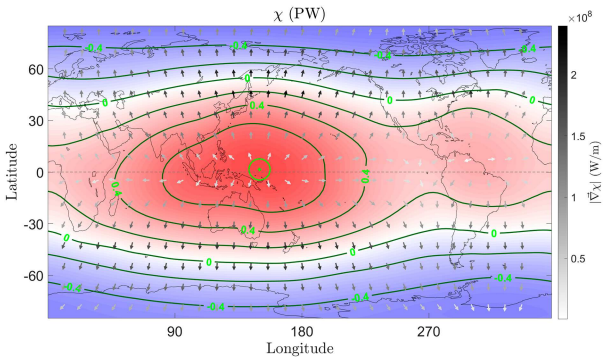

FIG. 1. The climatological atmospheric EFP, χ, calculated from the ERA5 data over the period 1979–2020. Red shades represent larger values of EFP, and blue shades represent lower values of EFP. The arrows point in the direction of divergent energy transport ($-\nabla\chi$), with darker arrows indicating stronger fluxes (corresponding to the gray color bar). Dark green contour lines indicate 0.2-PW intervals of the EFP, and the bright green cross and oval mark indicate its maximum.

maximum is a consequence of the heat capacity of land being much lower than that of the ocean. When insolation is strong in the Northern Hemisphere, there are larger surface energy fluxes from Asia than from the relatively cool oceans at the same latitudes. This extra energy input is exported from the region by the atmosphere, producing an EFP maximum. The location of the northern summer maximum repeats each year, rarely varying by more than 5° longitude or latitude. Note that the EFP maximum is largely over the Bay of Bengal rather than land, likely due to cloud shortwave effects decreasing the amount of sunlight reaching the continent's surface (Ramesh and Boos 2022).

As the insolation maximum moves southward in September–November, the EFP maximum diminishes and shifts to the south and east until it is over the equatorial west Pacific (approximately 5°N, 155°E), with most of this shift occurring between September and October. During December and January, the EFP maximum intensifies and remains over the west Pacific, decaying to become vanishingly small by April. Over the course of northern autumn and winter, the location of the EFP maximum becomes more variable; in December and January, it can be found anywhere from 10°S to 25°N in the west Pacific, while in February and March, it can be as far east as South America (not shown). The bottom panel of Fig. 2 summarizes this seasonal cycle, displaying the Indo-Pacific EFP maximum for each month in different colors. It shows that there are, broadly speaking, two states of the EFP: the maximum resides in South or Southeast Asia in northern summer and over the equatorial west Pacific in northern winter, with the major transitions during April/May and September/October.

Energy export and, therefore, EFP maxima are associated with deep atmospheric convection, which often leads to precipitation. To the extent that this is true, one expects precipitation maxima to be broadly collocated with EFP maxima. To study the correspondence between precipitation and the EFP, Fig. 2 shows the precipitation (smoothed by a simple moving mean over a 10° latitude by 10° longitude region) in each month contoured in blue. Precipitation has structure on much smaller scales than the EFP, due to topography and other complicating effects (e.g., Boos and Kuang 2010; Bergemann and Jakob 2016; Wei and Bordoni 2018; Baldwin et al. 2019), but on large spatial scales, the precipitation and EFP maxima broadly match over the seasonal cycle. In particular, there is an EFP maximum corresponding to the South Asian monsoon during northern summer (June–August) and intense precipitation collocated with the EFP maximum in the equatorial west Pacific from October through April. However, there are several places where precipitation is not well collocated with the EFP. For example, the South Asian monsoon is clear in the EFP (May) before it is in precipitation (June). Additionally, the precipitation maximum moves into the west Pacific (December) after the EFP maximum does (October). Over the seasonal cycle, this lag often appears as a widening of regions of high precipitation. For example, in June, the South Asian monsoon has begun, but there is still lots of precipitation in the equatorial west Pacific, a place where the EFP had a maximum in April. This lag between precipitation and energy export has been studied previously (Wei and Bordoni 2018) and is thought to be due to the seasonal cycle of gross moist stability, but for the purposes of this work, the EFP maximum is sufficiently well collocated with that of precipitation.

Previous studies have suggested that the Indo-Pacific precipitation zonal maximum follows the diagonal configuration of the low heat capacity regions of India, Indonesia, and Australia over the seasonal cycle (Heddinghaus and Krueger 1981; Meehl 1987, 1993) but did not test this hypothesis. In this study, we perform simulations and develop an analytic model to investigate the mechanism underlying the zonal movement of the EFP maximum and associated precipitation.

3. Idealized coupled atmosphere–ocean simulations

a. *Model setup*

Simulations are carried out using a coupled model based on the MITgcm (Marshall et al. 1997) in idealized configurations with and without a dynamic ocean. Simulations without a dynamic ocean are run for 150 years, while those with a dynamic ocean are run for 1000 years since the latter take much longer to reach a quasi-steady state. All diagnostics are computed based on the last 80 years of each simulation. The model configuration and some climatological solutions are shown in Fig. 3.

The model uses a cubed-sphere grid with approximately 2.8° horizontal resolution in both the atmosphere and the ocean (Adcroft et al. 2004). The atmospheric model has 26 pressure levels and idealized moist physics, a gray radiation scheme (Frierson et al. 2007), and water vapor feedback on longwave optical thickness (Byrne and O'Gorman 2013). It does not have clouds or shortwave absorption, so the planetary albedo is equal to the surface albedo, plotted in the top left of Fig. 3. The albedo is prescribed to depend only on latitude and to be asymmetric about the equator; it is slightly lower in the Northern Hemisphere, which therefore becomes warmer, shifting the ITCZ to the north. The continent is placed north of the equator

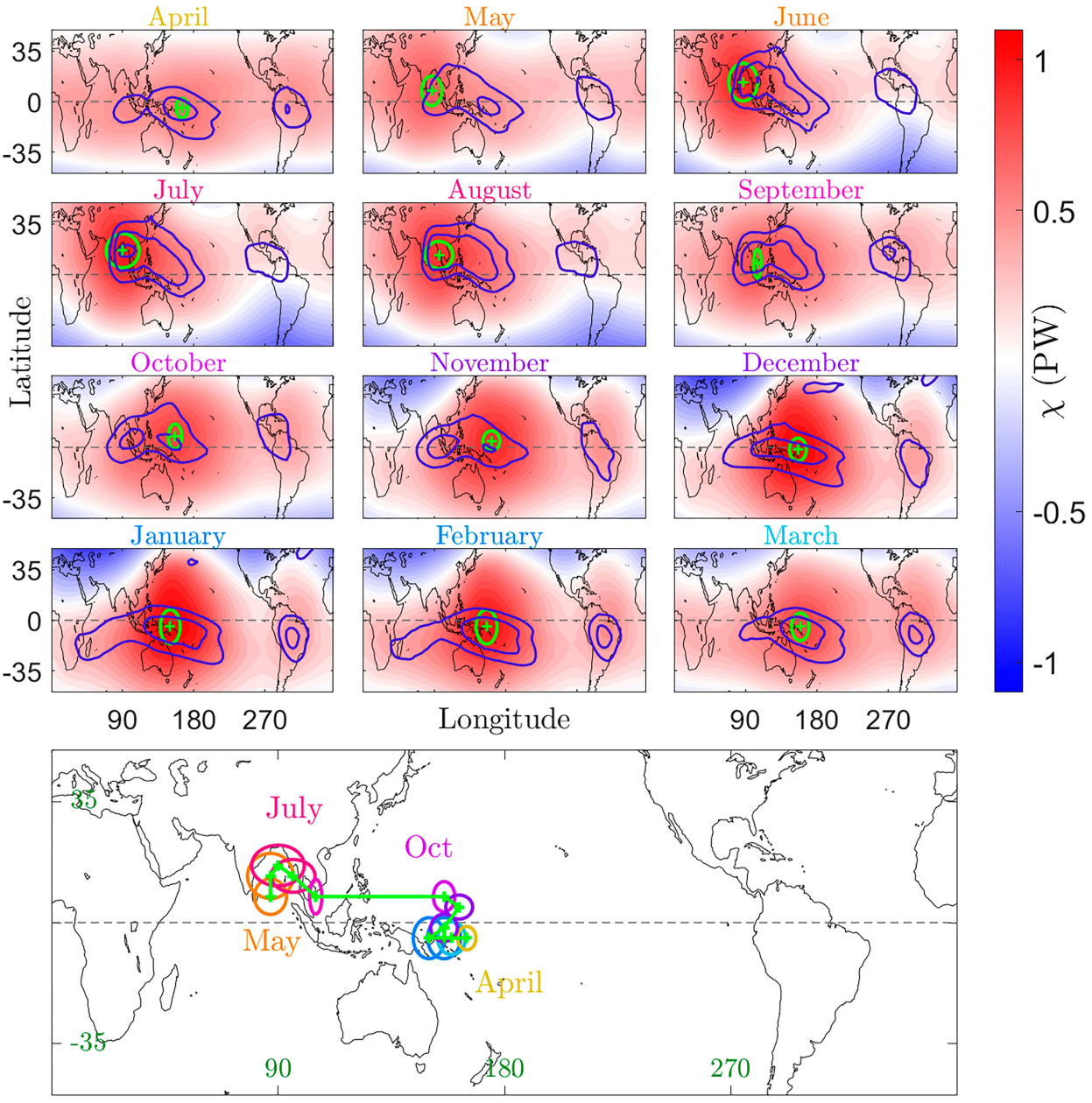

FIG. 2. Seasonal cycles of EFP (χ; red–blue color map) and smoothed precipitation (blue contours; ±10° longitude and latitude simple moving mean) in reanalysis data for each month. The maximum of the EFP in the Indo-Pacific region is marked by a green cross and a green oval. The ovals have a zonal radius corresponding to the zonal heat transport away from the maximum (3° longitude per 10^6 W m^{-1}) and a meridional radius corresponding to the meridional heat transport away from the maximum (1° latitude per 10^6 W m^{-1}). Note that in September–April, there is a maximum over the Americas that is not highlighted. The precipitation contours are at 5, 7, and 9 mm day^{-1}. The bottom panel shows the Indo-Pacific EFP maxima each month, color-coded by month and connected by green lines, with ovals half the size as those in the monthly panels.

(Fig. 3), so a warmer Northern Hemisphere causes the ITCZ to move over land in JJA, as observed in the Asian monsoon. The model has a seasonal cycle of insolation appropriate for a circular orbit with an obliquity of 23.45°.

The dynamic ocean has 15 vertical levels and a uniform depth of 3.4 km. The continental configuration consists of three infinitesimally thin ridges running south from the North Pole and a large landmass in the Northern Hemisphere, treated as a 2-m slab ocean (see the globe in Fig. 3). Two thin barriers stretching from the North Pole to 35°S separate the Atlantic basin from the others, and one reaching 30°S separates the Indian and Pacific basins. There is a gap between the continent and the barrier to its southeast to allow for an Indonesian Throughflow, preventing the development of a

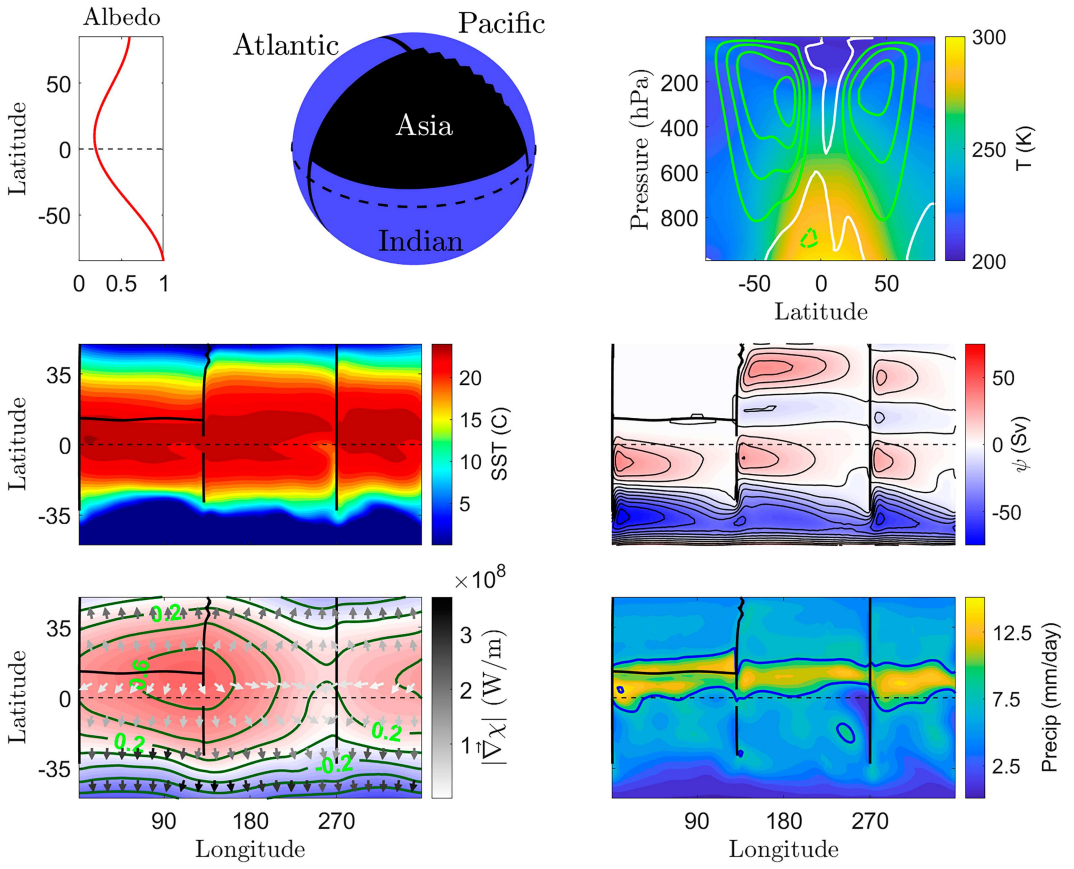

FIG. 3. Idealized atmosphere–ocean coupled model setup and the resulting climatological solutions. The top left shows surface albedo as a function of latitude, while the globe shows the continental configuration consisting of land (black; extending from 0°E to approximately 135°E) and ocean (blue). In all panels, dashed black lines represent the equator. Africa, the Americas, and Australia are represented as thin lines which block ocean flow. The Australian ridge (east of the Indian Ocean) reaches 30°S, while the other ridges reach 35°S. The top right shows zonal-mean atmospheric temperature (colors) as a function of latitude and pressure, as well as zonal-mean zonal wind, with the white line representing zero mean wind and the solid lines representing westerlies (contour interval 7 m s^{-1}). The middle row shows the annual mean SST (left) and the depth-integrated streamfunction of the ocean (right), where positive values indicate clockwise flow. Note that the SST is defined over the continent as it is treated as a slab ocean. The bottom row shows the climatological EFP (left), with arrows representing the divergent component of heat transport as in Fig. 1, and precipitation (right).

cold tongue in the Indian Ocean. Note that the northern part of the boundary between the continent and the Pacific is not a perfectly straight line due to the orientation of the polar face of the cubed sphere. To conserve freshwater, excess rain over the continent (i.e., the integral over the continent of precipitation minus evaporation) is distributed into the Atlantic basin.

This simple configuration allows us to study the Indo-Pacific zonal seasonal cycle in isolation from other complicating factors. For example, it helps distinguish the role of Asia from that of other landmasses, such as the Maritime Continent and Australia, the latter of which has been suggested as part of the origin of the observed zonal seasonal cycle (Heddinghaus and Krueger 1981; Meehl 1987, 1993; Chang et al. 2005).

In the simulation without a dynamic ocean, the continent is still represented by a 2-m slab, but the rest of the globe is represented by a 30-m slab ocean. Donohoe et al. (2014) found that slab ocean depth has a large effect on ITCZ position; 30 m is chosen to create a significant difference in heat capacity between the continent and the ocean. We compare 30-m slab ocean simulations with and without a continent to each other and to simulations with 18- or 24-m slab oceans. These comparisons are useful for isolating the controlling factors for the EFP shift from southern Asia to the western Pacific (see section 4).

Climatological solutions for the dynamic ocean simulation are shown in Fig. 3. The model produces Earth-like zonal-mean atmospheric temperatures, midlatitude jet streams, surface westerlies, Hadley cells, and tropical easterlies (top right). Sea surface temperatures (SSTs; middle left) are broadly similar to observations, decreasing away from the tropics and including a Pacific cold tongue. Note that poleward of roughly 40°S, the SSTs are below the freezing point of water, as there is no representation of sea ice or land ice in the model, and the prescribed albedo is higher in the Southern Hemisphere. Since our focus here is on the tropics, this does not affect our conclusions. The depth-integrated

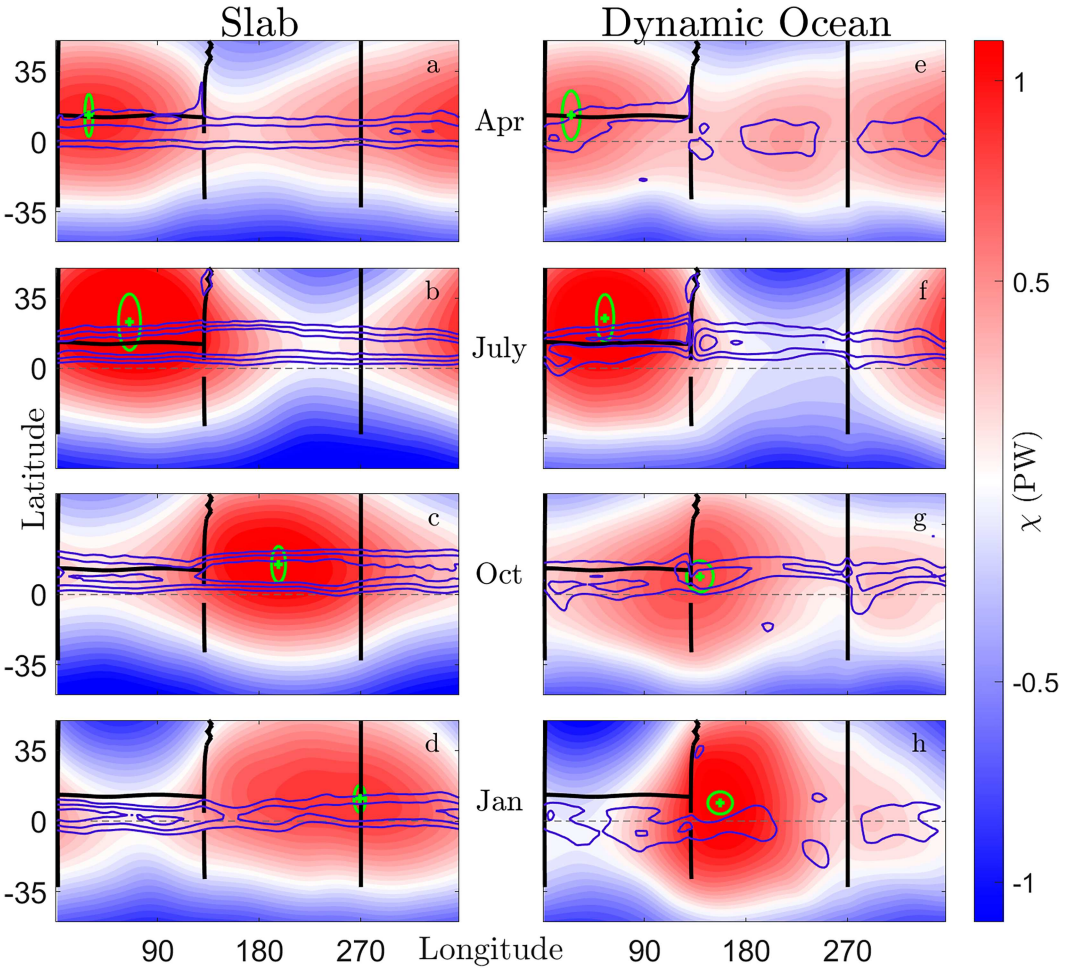

FIG. 4. The seasonal cycle of the EFP (χ; red–blue color map) and precipitation (blue contours, unsmoothed) in the (a)–(d) slab ocean and (e)–(h) dynamic ocean simulations. Months representative of northern (a),(e) spring (April), (b),(f) summer (July), (c),(g) autumn (October), and (d),(h) winter (January) are shown. The maximum of the EFP is marked by a green cross. The green oval has a zonal diameter proportional to the zonal heat transport away from the maximum (4° per 10^6 W m^{-1}) and a meridional diameter proportional to the meridional heat transport away from the maximum (1° per 10^6 W m^{-1}). The precipitation contours are at 10, 15, and 20 mm day^{-1}. The continent is in the top-left corner of each panel.

ocean circulation (middle right) is also as expected, with gyres responding to the surface wind stress, western boundary currents, and an Antarctic Circumpolar Current.

The climatological EFP broadly resembles that of Earth (bottom left of Fig. 3 versus Fig. 1), transporting energy meridionally away from the tropics and zonally away from the southeast corner of Asia. The maximum near South America is not captured, as there is no continent there. Last, the model has a well-defined single ITCZ (bottom right), with zonal asymmetries related to the continent and the Pacific cold tongue.

We now discuss the seasonal cycle in simulations with and without an active ocean.

b. *Simulated seasonal cycles*

In the slab ocean simulation (left column of Fig. 4), precipitation and EFP maxima move meridionally with the seasons, reaching their northernmost positions in July and their southernmost positions in January. This, together with the presence of the zonally asymmetric continent, results in zonal asymmetries over the course of the year. As with the reanalysis data in Fig. 2, we begin our description of the seasonal cycle in April (Fig. 4a) when the ITCZ overlaps with the continent (i.e., the shallow part of the slab ocean). The low heat capacity of the continent leads to a warmer surface and enhances energy flux into the atmosphere, creating a zonal maximum in the EFP (green cross in Fig. 4a). In addition, the ITCZ extends further poleward over land than over the ocean (cf. longitudes < 130°E and 130°–270°E), similar to the South Asian monsoon (Fig. 2). In the following months, the EFP and precipitation anomalies (relative to the zonal mean) propagate eastward. In July (Fig. 4b), the EFP maximum is centered well north of the continental boundary (23°N) and has moved

to about 60°E. Meanwhile, precipitation has intensified, with the largest changes over the continent and the west Pacific. This offset between the precipitation and EFP maxima will be discussed further in section 4. In October (Fig. 4c), the EFP maximum is further south, near the equator, and is significantly east of the continent, over the central Pacific. The precipitation anomaly tracks the EFP maximum and is most intense over the Pacific basin. Between October and January (Fig. 4d), the EFP maximum decreases in amplitude and spreads out zonally but continues to move east and reaches all the way to the east Pacific and west Atlantic. The precipitation anomaly associated with the EFP maximum has mostly disappeared, and another precipitation anomaly, possibly caused by the strengthened Hadley cell moving energy toward the cold continent, has appeared south of the equator in the continental sector. While this precipitation is of general interest, we are not concerned with it in the present study.

In the dynamic ocean simulation (right column), the EFP maximum and precipitation move north and south with the solar forcing over the course of the year. Just as in the slab ocean simulation, an EFP maximum forms in April over land and moves east during JJA (Figs. 4e,f). There are, however, significant differences between the simulations. The precipitation in the dynamic ocean simulation has smaller-scale features but, on large scales, again broadly follows the EFP, moving north in the summer, moving southeast in the winter, and being concentrated over the continent in July. Note that just as in the slab ocean simulation, the precipitation in July is centered over the eastern part of the continent and the west Pacific, rather than over the center of the continent. Another difference between the simulations is that the dynamic ocean EFP maximum in January is larger than that of the slab ocean, presumably because the ocean brings energy toward the west Pacific and warms the atmosphere in that region, and this energy is then exported via the Walker circulation. Perhaps the most notable difference between the simulations is that the EFP maximum in the dynamic ocean case does not propagate as far eastward. In April, the zonal positions of the EFP maxima are similar with or without an active ocean (Figs. 4a,e; 33° and 27°E), and in July, they are close but not identical (Figs. 4b,f; 69° and 57°E). In October, however, the slab ocean EFP maximum is already in the central Pacific, while that of the dynamic ocean remains near Asia (Figs. 4c,g; 199° and 139°E). By January, the slab ocean maximum has moved all the way across the Pacific and into the Atlantic, while in the dynamic ocean case, the maximum remains stalled in the west Pacific (Figs. 4d,h; 271° and 161°E).

We highlight the differences between the slab and dynamic ocean simulations in Fig. 5, which shows the seasonal cycles of the Indo-Pacific EFP maxima in reanalysis data and the two simulations. In reanalysis, the maximum is over India and/or the eastern Indian Ocean for almost half the year (May–September), then migrates to the west Pacific, and remains there (top panel). In the slab ocean simulation (middle panel), an EFP maximum forms over the continent in April, moves northeast until July, and then moves southeast for most of the remainder of the year. In the dynamic ocean case (bottom panel), an EFP maximum once again forms over the continent in April and moves northeast until July. This maximum also

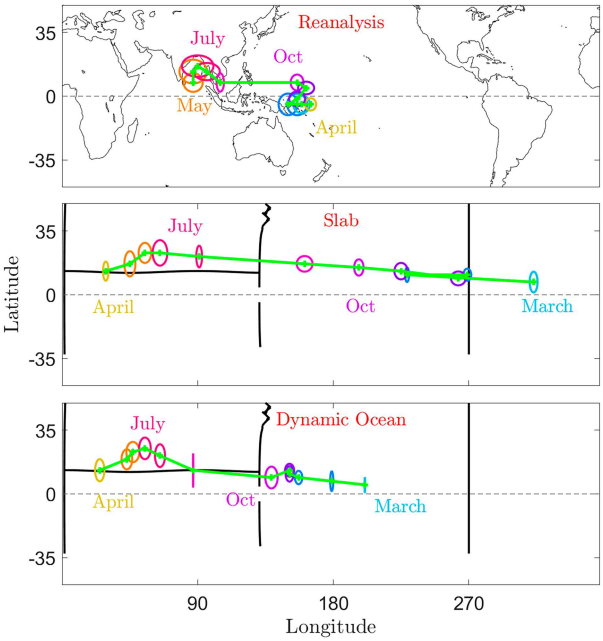

FIG. 5. Comparison of the seasonal cycles of the EFP maximum in (top) reanalysis data and two simulations [(middle) slab ocean and (bottom) dynamic ocean]. Each panel shows the maxima, as in Figs. 2 and 4, with different colors corresponding to each month. The maxima are marked by green crosses and connected via green lines (without the April–May connection in the reanalysis panel and without the March–April connection in the simulation panels). The meridional radii for the ovals are 1° per 4×10^6 W m^{-1} of meridional heat export, and the zonal radii are 1.5° (reanalysis) or 2° (simulations) per 10^6 W m^{-1} of zonal energy export. The black lines show the continental configuration.

moves eastward over the course of the year but at a slower speed than in the slab ocean case, and it has died away by the time it reaches the central Pacific. Specifically, the dynamic ocean maximum arrives in the west Pacific at a later time than in the slab ocean, and it does not move out of the west Pacific until February/March when the anomaly has decayed significantly. The simulations differ from the reanalysis in April—the simulated EFP maxima are over the continent rather than the west Pacific—perhaps due to the highly simplified representation of the continent's surface or geometry.

To summarize, in all three cases (reanalysis, slab ocean simulation, and dynamic ocean simulation), an EFP maximum forms over land during the Northern Hemisphere spring, moves east during JJA, and shifts to the west Pacific in September or October. In the slab ocean case, the EFP maximum continues to move eastward for most of the year, crossing the entire Pacific. In the dynamic ocean and reanalysis cases, by contrast, the EFP maximum stalls over the west Pacific. While the meridional seasonal cycles of the EFP and precipitation follow the insolation maximum, the mechanisms of the zonal seasonal cycles are unclear. We now develop a simple model for the eastward movement of the EFP and energy anomalies and go on to discuss the role of the dynamic ocean in preventing the anomaly from crossing the Pacific.

4. Model for the propagation of energy anomalies

We now propose a mechanism for the eastward movement of the EFP anomaly and its associated precipitation. It has similarities to the "moisture mode" theories that have been developed to describe the Madden–Julian oscillation (Raymond and Fuchs 2009; Sobel and Maloney 2013; Adames and Maloney 2021; Wang and Sobel 2022), in that it is a mechanism for an eastward-propagating anomaly in the tropics, with energy stored mostly in the form of latent heat. Moisture mode theory, however, treats SSTs as fixed, so surface fluxes are controlled entirely by near-surface wind speeds, while in this case, changes in SST are essential, and the near-surface wind is held fixed. Due to the relevance of the monsoon for the observed behavior, we label this propagating signal a "monsoonal mode." We begin by describing the monsoonal mode qualitatively and then develop an analytic model to explore what controls its speed and rate of growth or decay. Full details of the analytic model are given in the appendix.

a. *Qualitative description*

To discuss the monsoonal mode, we consider an idealized setting in which there is a zonally confined continent of low heat capacity in one hemisphere. In summer, the land warms, heating near-surface air above it and forming an EFP maximum. Advection of this energy eastward by near-surface westerlies, and advection of less energetic air from the ocean to the west of the continent, leads to the eastern part of the continent being relatively warm (Chou et al. 2001; Privé and Plumb 2007a; Zhou and Xie 2018) and having more precipitation (e.g., Fig. 4b). When the energetic continental air is advected over the ocean, it suppresses air–sea fluxes, as the air–sea energy difference is decreased. This increases local SSTs because less energy is lost to the atmosphere. When the continent cools down in autumn, the increased SSTs of the nearby ocean persist. This causes the anomaly of surface temperature to move from the continent to the ocean.

To summarize, warming over land triggers the monsoonal mode, and it continues to propagate over the ocean via the following mechanism:

- A surface temperature anomaly is at position x.
- The boundary layer air above the warm surface becomes more energetic and is advected eastward to $x + \Delta x$.
- Air–sea fluxes are suppressed due to a decreased ocean–atmosphere energy difference at $x + \Delta x$.
- The surface temperature at $x + \Delta x$ increases due to decreased surface fluxes.

In the system being studied here, the anomaly first develops because of the low heat capacity of Asia and moves eastward into the west Pacific, so we refer to it as the Indo-Pacific monsoonal mode. However, a monsoonal mode could be triggered by other means or in other regions.

A schematic of the monsoonal mode mechanism is shown in Fig. 6a. In July (left), the warm continent leads to large surface fluxes and the resulting high MSE air is advected to the east. This energetic air, now over a relatively cool ocean, suppresses surface fluxes because of the reduced air–sea temperature difference, making west Pacific SSTs anomalously warm. In September (right), the warm west Pacific SSTs remain, leading to enhanced surface fluxes there. The warmed air is then advected further to the east, continuing the propagation of the monsoonal mode.

The schematic is motivated by anomalies diagnosed from slab ocean simulations such as those shown in Fig. 6b. The quantities are calculated as the difference between the previously discussed slab ocean simulation and one without a continent. In July, in the simulation with a continent, surface fluxes (Fig. 6b, left column, top row) are very large over Asia, up to 100 W m^{-2} larger than those of the simulation without a continent. Consequently, the atmospheric energy (middle column) is larger over the eastern part of the continent and the west Pacific due to low-level westerlies. The surface fluxes over the Pacific are therefore lower than in the simulation with no continent, leading to relatively warm SSTs (right column). In September (bottom), the high Pacific SSTs remain, leading to anomalously large surface fluxes in the west Pacific. Note that there is no ocean advection in either simulation and they have the same solar radiation, so this difference in SST is due to atmospheric advection. In both July and September, the EFP maximum (green oval) is in the center of the region of excess surface flux, not that of excess energy, because the EFP depends on energy flux, not energy content. As the atmosphere is moving energy away from the area of excess surface fluxes, that is the position of the EFP maximum.

The vertical structure of the monsoonal mode in the slab ocean simulation is shown in Fig. 7. Relevant quantities are calculated as composites, centered around the EFP maximum, averaged over the year, and with the zonal mean removed. The vertical structure of MSE in the composite (Fig. 7a) does not change very much with respect to longitude, and the column-integrated MSE has a maximum of about 70° east of the EFP maximum. The vertical velocity at around 615 hPa (arrows, shown without removing the zonal mean) also peaks approximately 70° east of the maximum though there is ascent everywhere in the tropics. This matches the location of enhanced precipitation in Fig. 4; e.g., in July, the EFP is centered over the center of the continent, while the maximum precipitation occurs along the continent's eastern coast. The zonal wind (shown as a black line, without removing the zonal mean) has some vertical structure but is positive (westerly) everywhere below about 300 hPa due to the northward Hadley return flow being acted on by the Coriolis effect. Note that this is true only in the slab ocean simulation: Changes in the wind with a dynamic ocean are discussed in section 5. The SST (Fig. 7c), like the MSE, is at a maximum about 70° east of the EFP maximum. However, the MSE maximum is offset slightly to the east relative to the SST maximum (vertical line in all panels), reducing surface fluxes (Fig. 7b) east of the energy anomaly and enhancing surface fluxes to the west. In other words, the atmospheric energy anomaly is slightly downwind (east) of the ocean energy anomaly, so surface fluxes are suppressed downwind and amplified upwind (west). As the EFP depends only on net energy input (NEI) to the atmosphere, its maximum is upwind of the atmospheric MSE maximum. However, deep convection (and therefore

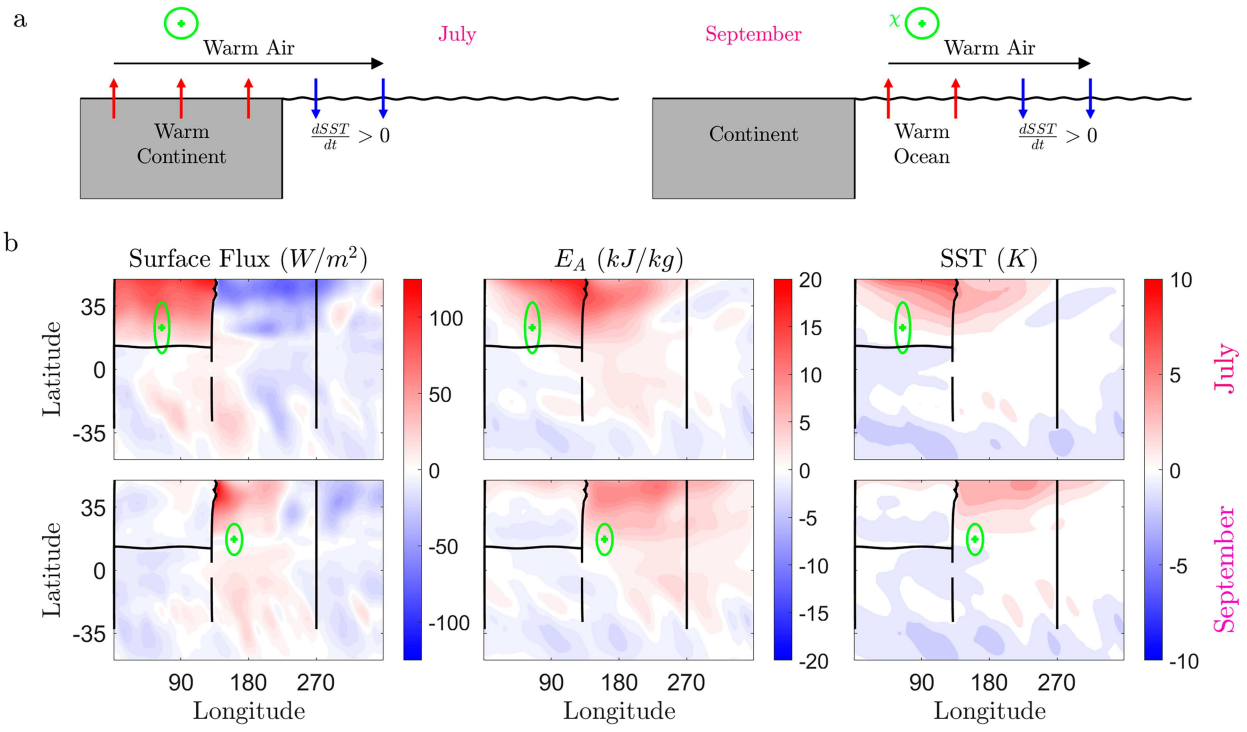

FIG. 6. (a) Schematics of the mechanism behind the eastward propagation of the monsoonal mode for (left) July and (right) September. Vertical arrows represent surface fluxes, and horizontal arrows represent horizontal advection. The positions of the EFP maxima are shown by green circles and are upstream of the MSE anomaly. (b) Computed anomalies of (left) surface energy fluxes, (middle) low-level moist static energy, and (right) SST. The top row shows July (representative of northern summer), and the bottom row shows September (autumn). Each anomaly is calculated as the (monthly mean) difference between a simulation with a continent and one without (both with no ocean dynamics). The position of the EFP maximum from the simulation with a continent is shown by the green cross, and the size of the oval indicates the magnitude of the energy flux, with the same radii scales as in Fig. 4.

precipitation) depends directly on low-level atmospheric MSE, so it is downwind (east) of the EFP maximum.

b. *Analytical model for the monsoonal mode*

We now study an idealized model of the monsoonal mode in a simplified system with representations of atmospheric advection, surface fluxes, outgoing longwave radiation, and mixing processes. A detailed derivation and discussion of the system is in the appendix; here, we present the governing equations and their solution:

$$\frac{\partial}{\partial t}T + U_{\mathrm{BL}}\frac{\partial}{\partial x}T = \frac{\mathrm{SST} - T}{\tau} - \frac{T}{\tau_R} + \kappa_{\mathrm{FT}}\frac{\partial^2}{\partial x^2}T, \tag{3}$$

$$\frac{\partial}{\partial t}\mathrm{SST} = -\frac{C_A}{C_O}\frac{\mathrm{SST} - T}{\tau} - \frac{\mathrm{SST}}{\tau_R}. \tag{4}$$

The first equation is a statement of conservation of energy for the atmosphere, where T is a boundary layer temperature anomaly, assumed to be proportional to the vertically integrated atmospheric energy anomaly via a constant heat capacity C_A (see discussion in the appendix). As we wish to study a zonal anomaly, T is a function of x (longitude) and t (time) and should be thought of as the difference between a system with a continent and one without. The terms in the atmospheric energy budget are advection, surface fluxes, radiation, and free tropospheric mixing, represented by a diffusive term. Advection is set by U_{BL}, the boundary layer zonal wind, and the surface flux (first term on the right side) is proportional to the difference in temperature between the surface and atmosphere (i.e., SST $-$ T) via a surface flux time scale τ. The radiative energy loss is proportional to the atmospheric temperature divided by a radiative time scale τ_R. The free troposphere (FT) is assumed to mix energy with an effective diffusivity of κ_{FT} because tropical circulations tend to smooth energy gradients (Craig and Mack 2013; Hottovy and Stechmann 2015; Ahmed and Neelin 2019).

The second equation is a slab ocean energy budget, with ocean energy proportional to sea surface temperature (SST) via the ocean heat capacity C_O. Just as with the atmospheric temperature, SST is the anomalous sea surface temperature and should be thought of as the difference between a system with a continent and one without. The only sources or sinks of ocean temperature are surface fluxes and radiation, with analogous expressions to those for the atmosphere. Note that the surface flux term is modulated by the ratio of atmosphere to ocean heat capacities, as the same amount of energy (but not temperature) is leaving the ocean as is entering the atmosphere.

We seek solutions of the following form:

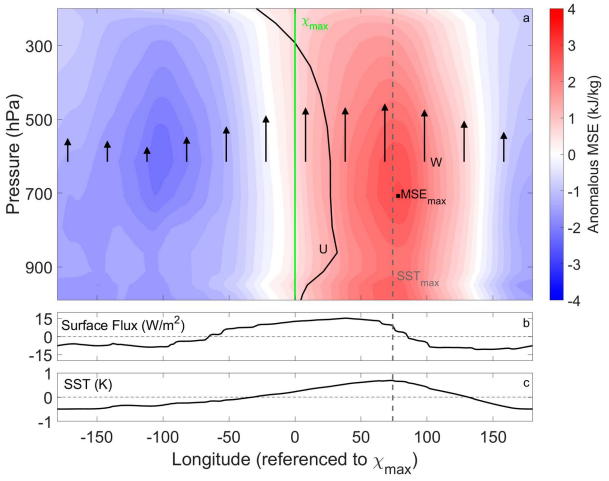

FIG. 7. A composite of the monsoonal mode in the slab ocean simulation, showing the vertical structure of MSE, the surface flux, and SST. The zonal anomaly of MSE is in color, while the vertical black line is the profile of zonal velocity at the EFP maximum. The maximum value of the zonal velocity is 3.2 m s^{-1}, and zero wind corresponds to the green line. The arrows represent the vertical velocity at ~615 hPa, and the location of the EFP maximum, around which the composite is taken, is shown as a green line. The zonal anomalies of the surface flux and SST are shown in the bottom panels. The longitude of the maximum SST (dashed gray line) and the position of the maximum MSE (black square) are marked.

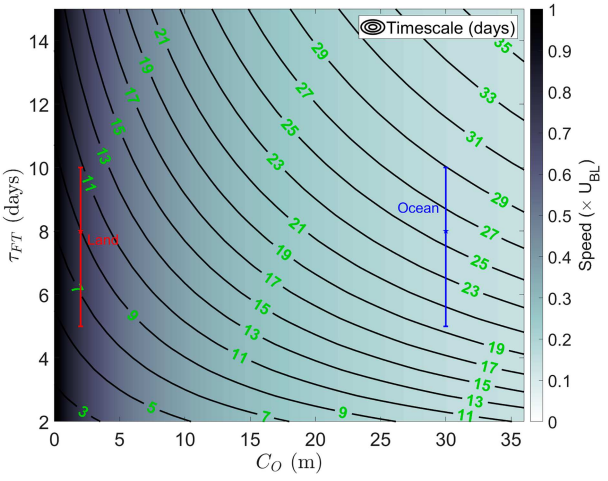

FIG. 8. The dependence of phase speed as a fraction of U_{BL} (shaded) and decay time scale (contours) on the ocean heat capacity C_O and free troposphere diffusive time scale τ_{FT} in Eq. (5). Approximate locations in phase space over the land and ocean in the slab ocean simulation are marked, with uncertainties given by an 80% confidence interval on τ_{FT}. For this figure, τ_R is set equal to 56 days, C_A is set to the heat capacity of a 6-m slab ocean, and the wavenumber k is taken to be 2×10^{-7} 1 m^{-1} based on the width of the continent. These values are discussed in detail in the appendix and summarized in Table A1.

$$(T, \mathrm{SST}) = (\tilde{T}, \widetilde{\mathrm{SST}})\exp[i(kx - \omega t)],$$

where $\tilde{T}$ and $\widetilde{\mathrm{SST}}$ are complex amplitudes for the temperature of the atmosphere and ocean, respectively. A dispersion relation is calculated by setting the determinant of the relevant matrix to zero (details in the appendix). A useful and accurate approximate solution can be obtained by noting that the surface flux time scale is short (~3 days) compared to the other time scales involved (see Table A1), giving

$$\frac{\omega}{k} \approx U_{\mathrm{BL}} \frac{C_A}{C_A + C_O} - \frac{i}{k}\left(\frac{1}{\tau_R} + \frac{1}{\tau_{\mathrm{FT}}}\frac{C_A}{C_A + C_O}\right). \qquad (5)$$

Equation (5) can be interpreted as follows. The energy in the atmosphere is $C_A T$, while the energy in the ocean is C_OSST. With a short surface flux relaxation time scale, i.e., as SST $\to T$, the total energy is $(C_A + C_O)T$. Therefore, the ratio $C_A/(C_A + C_O)$, which appears twice in Eq. (5), is the fraction of the energy anomaly stored in the atmosphere. Since advection by low-level wind acts only on atmospheric energy, the real part of the phase speed is the wind speed U_{BL} multiplied by this ratio. Since $C_O > 0$, the anomaly does not move at U_{BL} but at a slower speed. Similarly, the effect of free troposphere diffusion [controlled by $\tau_{\mathrm{FT}} \equiv 1/(k^2\kappa_{\mathrm{FT}})$, a free troposphere diffusive time scale] is modulated by the same expression. Meanwhile, radiation causes both the atmosphere and the ocean to lose energy, so its contribution to the decay rate does not depend on the heat capacities.

Figure 8 shows the implied phase speed (ω/k) as a function of C_O and τ_{FT}, with real and imaginary components representing the propagation speed and growth/decay rate, respectively. As discussed above, the propagation speed (shaded) depends strongly on C_O, as heating the ocean takes longer when its heat capacity is larger, slowing down the monsoonal mode. The time scale of decay (contoured) increases with both τ_{FT} and C_O: If the atmosphere diffuses energy slowly or the ocean stores more energy, the monsoonal mode decays more slowly.

To calculate the decay and propagation time scales, it is necessary to determine C_A. Although the heat capacity of a dry column of air is much smaller than that of an ocean column, moist atmospheric columns can have higher heat capacities. As described in the appendix, to estimate C_A, we calculate the constant of proportionality between column-integrated energy and boundary layer temperature in the tropics of the slab ocean simulation. We find that the tropical atmosphere has a heat capacity of ~2.4×10^7 J m^{-2} K^{-1}, roughly that of a 6-m slab ocean, in agreement with Cronin and Emanuel (2013).

We can use our simple model to estimate the speed of the monsoonal mode when it is over the continent (depth of 2 m, $C_O \sim 8.3 \times 10^6$ J m^{-2} K^{-1}) or the ocean (depth of 30 m, $C_O \sim 1.2 \times 10^8$ J m^{-2} K^{-1}). Using Eq. (5), we obtain propagation speeds of 2.25 and 0.5 m s^{-1} (for $U_{\mathrm{BL}} = 3$ m s^{-1} and C_A based on a 6-m slab ocean), while the decay time scales are 9 and 26 ± 2 days (for $\tau_{\mathrm{FT}} = 8$ days), respectively. Note that these decay estimates are appropriate for the slab ocean simulation only; the mechanism responsible for the decay of the monsoonal mode in the dynamic ocean simulation will be discussed in section 5.

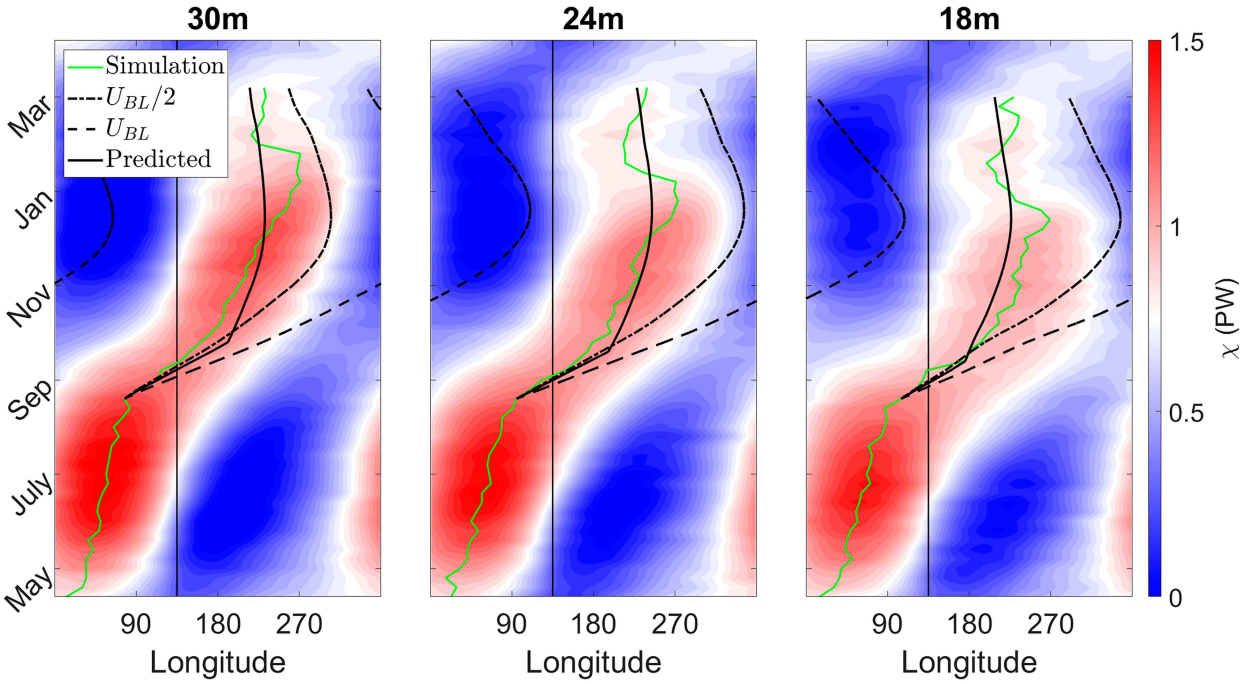

FIG. 9. Hovmöller diagrams of EFP anomaly propagation at 15°N from three simulations with slab ocean depths of (left) 30 m, (center) 24 m, and (right) 18 m. The longitudinal positions of the EFP maxima are highlighted in green. Black lines indicate the trajectory of the EFP maximum if it had moved at $U_{\mathrm{BL}}/2$ (dot–dashed), U_{BL} (dashed), or at the predicted phase speed (solid) according to our theory. The predictions begin when the monsoonal mode is no longer directly forced by insolation (i.e., at the end of summer) and end when the anomaly has decayed to a value < 0.8 PW. To calculate the predicted phase speed, the atmospheric heat capacity is taken to be that of 6 m of water, while the ocean heat capacity over the continent is set to 2 m of water when the zonally anomalous EFP is positive over land. The vertical black line at longitude 135° represents the border of the continent.

To assess the predictive capability of our analytic model, Fig. 9 shows the movement of the Indo-Pacific monsoonal mode in three simulations with different slab ocean depths. We compare the simulated monsoonal mode's speed to U_{BL}, $U_{\mathrm{BL}}/2$ (the speed if $C_A = C_O$ and $\tau \to 0$), and the speed predicted from Eq. (5), where U_{BL} is the boundary layer zonal wind diagnosed from the simulation at 975 hPa at the position of maximum atmospheric energy. We see that our simple model matches the slab ocean simulations well for most of the year and across several slab ocean depths. Importantly, the predicted speed explains the slowdown of the anomaly when it moves from the continent to the ocean.

5. Role of the dynamic ocean

We now turn to the role of the dynamic ocean in preventing the propagation of the Indo-Pacific monsoonal mode across the Pacific. It is clear that ocean dynamics have a significant impact on the position of the EFP maximum in northern fall and winter, as the slab ocean simulation is quite different from reanalysis and the dynamic ocean simulation in those seasons (Fig. 5). This is due to the Walker circulation/cold tongue system controlled by the Bjerknes feedback (Bjerknes 1969). In the annual mean, equatorial easterlies across the Pacific bring warm surface water to the west, causing upwelling and lower SSTs in the east. The Walker circulation, with air rising in the warm west Pacific and descending in the cold east Pacific, arises from this zonal SST gradient and strengthens the equatorial easterlies, completing a positive feedback loop known as the Bjerknes feedback. However, this does not occur without a dynamic ocean and accounts for the differences between the slab and dynamic ocean simulations both in SST and near-surface winds in the equatorial Pacific. These factors influence the position of the EFP maximum and precipitation during northern fall and winter.

Figure 10 shows the sign of zonal near-surface winds and the net energy input into the atmosphere in reanalysis (top row), the slab ocean simulation (middle), and the active ocean simulation (bottom) for September (left column) and November (right column). In September, the EFP maximum is in a region of westerlies in all three cases and therefore moves east (see Fig. 5). However, the effect of the cold tongue is already visible, as the net energy input to the atmosphere is significantly higher in the equatorial east Pacific in the slab ocean case (middle row) than in the other two. This leads to an EFP maximum that is further east in the slab ocean simulation.

By November, the EFP maximum has moved to the Pacific in all three cases (~220°–230°E in the slab ocean simulation and ~150°–160°E in reanalysis and the dynamic ocean simulation). In the slab ocean case, it is still in a region of mean westerlies (as there is no Walker circulation) and so moves

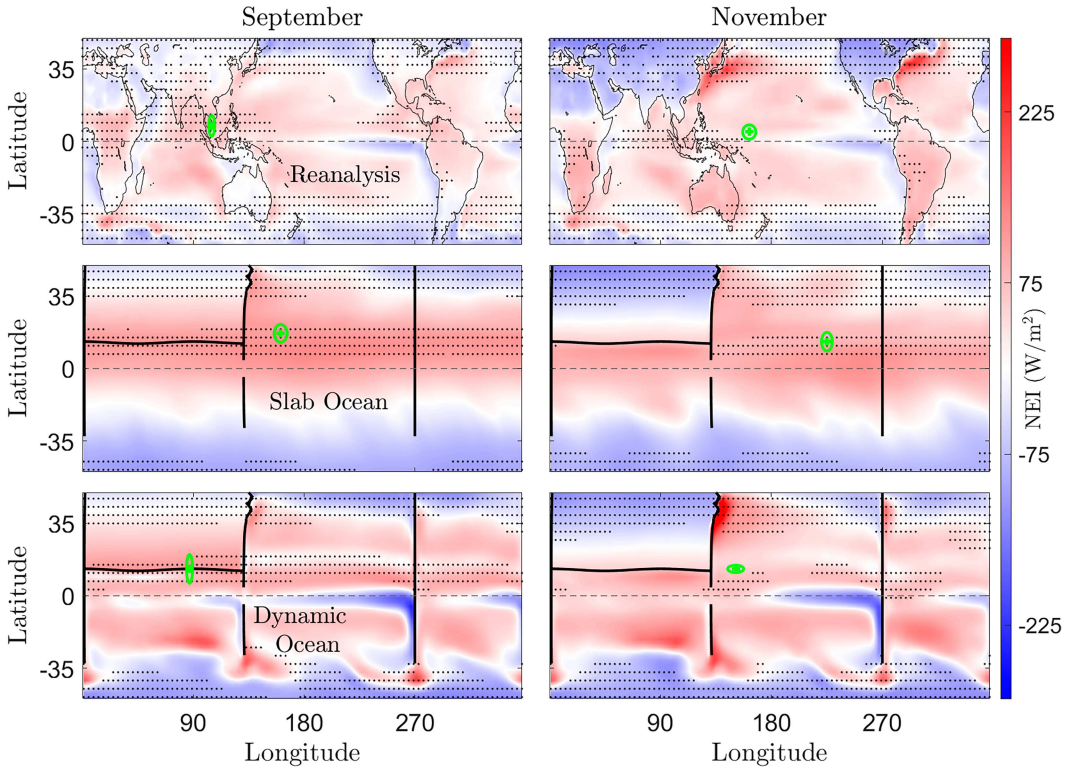

FIG. 10. The NEI (color) into the atmosphere (positive indicates atmospheric warming) in (top) reanalysis, (middle) the (30 m) slab ocean simulation, and (bottom) the dynamic ocean simulation for (left) September and (right) November. Stipples indicate regions of westerly wind at ~900 hPa. The EFP maxima are marked with a green cross and oval.

east in the following months. In reanalysis and the dynamic ocean simulation, however, the EFP maximum is in a region of (mostly) mean easterlies or little mean wind and thus stops moving. Additionally, the net energy input in the east Pacific is much lower in these cases, so, even if there were westerlies, the maximum would almost certainly not be over the cold tongue. It is worth noting that differing wind directions as a function of height may affect the movement of the monsoonal mode, but the near-surface winds are the most relevant as they control the air–sea temperature difference.

The importance of the Walker circulation/cold tongue system can also be seen by considering how the seasonal cycle of the EFP changes during El Niño–Southern Oscillation (ENSO). During El Niño events, i.e., when the cold tongue is weaker and westerlies extend into the central Pacific, the winter EFP maximum is further east than during La Niña events or the climatological mean (Boos and Korty 2016). We show this in Fig. 11 with an ENSO longitude index (ELI), based on Williams and Patricola (2018), calculated as the average SST anomaly (relative to the climatological mean) from 140° to 260°E and from 5°S to 5°N, weighted by longitude. Intuitively, ELI is positive when the east Pacific is relatively warm, and it is negative when the west Pacific is relatively warm. In the average across positive ELI years, the winter EFP maxima are further east, while during negative ELI years, the winter EFP maxima are further west.

In summary, a combination of the lower SSTs of the Pacific cold tongue and the easterlies of the Walker circulation, a feedback which exists only when the ocean transports energy, blocks the eastward movement of the EFP maximum, leading to the seasonal cycles shown in Figs. 2 and 5.

6. Conclusions

In this study, we have applied an energetic framework for ITCZ behavior to explore the zonal seasonal cycle of tropical precipitation in the Indo-Pacific. In reanalysis data, an EFP maximum and associated enhanced precipitation emerge in northern spring/summer over South Asia and move southeast to the west Pacific during northern autumn and winter. In an idealized simulation without a dynamic ocean, a low heat capacity continent initiates EFP and precipitation zonal maxima during northern spring. These maxima propagate east via advection by near-surface westerlies and are sustained by coupling between low-level MSE and SST. In February and March, the anomalies decay, and the system becomes more zonally symmetric. An analytic model captures the eastward movement of this "Indo-Pacific monsoonal mode" and shows that the speed of propagation is modulated by the ratio of atmosphere to atmosphere + ocean heat capacity. With a dynamic ocean, the migration of the EFP maximum is stopped in the west Pacific due to the Bjerknes feedback between the Pacific cold tongue and equatorial easterlies, leading to a seasonal cycle matching that of reanalysis.

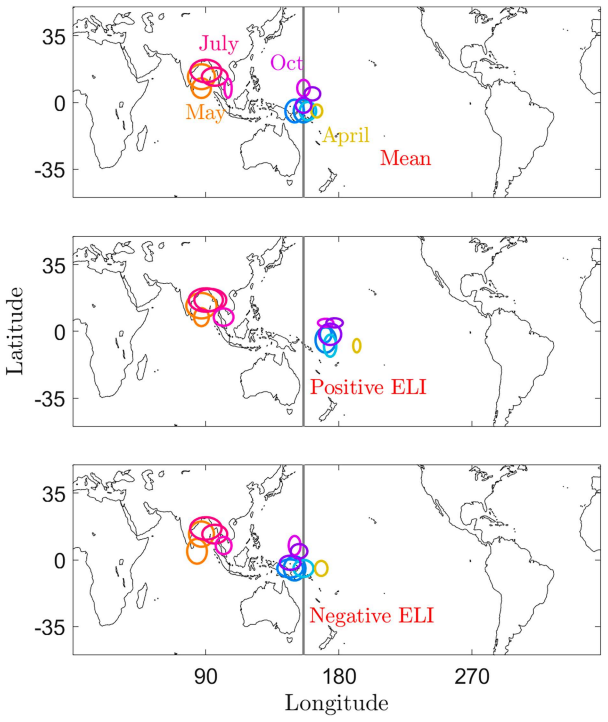

FIG. 11. The seasonal cycle of EFP migration in reanalysis data in the (top) climatological mean, (middle) positive (>0.5) ELI years, and (bottom) negative (<−0.5) ELI years. Each panel shows an oval around the EFP maximum in each month. As in previous figures, the size of each oval is proportional to the energy export from the EFP maximum. The color of the contour for each month matches those in Figs. 2 and 5. The gray vertical line shows the October–March climatological mean zonal position of the EFP maximum.

We believe that our study is relevant to a number of topical and important problems in tropical meteorology. First, although our focus has been on the creation and propagation of energy anomalies, this work has important implications for understanding patterns of tropical precipitation. Other variables, such as subcloud entropy, may be better predictors of local precipitation (e.g., Privé and Plumb 2007a; Harrop et al. 2019), but the energetic framework allows us to place precipitation anomalies in a global-scale context. The detailed patterns of precipitation are complicated by the presence of orography, surface properties, and other local effects, but the EFP follows broad features of precipitation patterns and is much cleaner. Second, this study shows the importance of ocean dynamics in setting tropical precipitation patterns, not only in damping meridional ITCZ shifts (e.g., Green et al. 2019) but also in the zonal seasonal cycle of peak precipitation. Third, our proposed mechanism provides an elegant interpretation for the seasonal asymmetry of precipitation in the Indo-Pacific sector, without invoking the specific continental geometry of the region (Heddinghaus and Krueger 1981; Chang et al. 2005). Specifically, the idea that a monsoonal mode forms over Asia, travels east, and then decays is a straightforward explanation for the seasonal cycles of precipitation over the equatorial Maritime Continent and SST of the west Pacific (i.e., that the west Pacific is warmest during northern fall).

Despite these insights, many questions remain. While the simulations presented here capture the broad patterns of tropical precipitation, they are highly simplified. In the real world, land moisture limitations, surface albedo variations, continental geometry, orography, and cloud feedbacks all play roles in controlling precipitation. For example, the influence of the Sahara on tropical precipitation is no doubt significant but was not studied here. These effects can often be understood in terms of the energetic perspective, but not always. Work on these topics may help shed light on the difference between the locations of precipitation and the energy flux potential maxima discussed in reference to Fig. 2.

Another possible avenue of future research is the relationship between energy transport and aspects of the ITCZ other than position. For example, the width and amplitude of the ITCZ have been studied (e.g., Byrne and Schneider 2016) but rarely in the presence of a dynamic ocean (Donohoe et al. 2019, 2022). ITCZ variability (Popp et al. 2020), both in terms of its position and amplitude, is also of great relevance to society but poorly understood. Another use of the 2D energy framework is comparing the current climate to past and future ones. Precipitation in different climate states may be predicted via changes in the EFP that depend on the continental configuration or surface properties such as albedo and moisture content (e.g., Boos and Korty 2016).

Future work on the zonal seasonal cycle may also illuminate why the ascending branch of the Walker circulation is over the Maritime Continent in the annual mean (e.g., Wu et al. 2021). Our work suggests that this is perhaps because it is over South Asia during JJA and over the west Pacific during DJF.

Last, the idea of a monsoonal mode may provide insight into the onset and decay of monsoons, especially that of South Asia (Wang et al. 2004; Abe et al. 2013; Ma et al. 2019; Zhou et al. 2019; Geen et al. 2019; Recchia et al. 2021). Traditionally, the beginning and end of monsoon seasons have been thought of as meridional shifts of the ITCZ. However, as we have shown here, the onset of the South Asian monsoon can be seen as the formation of an atmospheric energy anomaly, and its decay can be seen as the zonal propagation of an annual monsoonal mode.

Acknowledgments. P. J. Tuckman was supported by the Rasmussen Fellowship, a graduate fellowship for the Department of Earth, Atmospheric, and Planetary Sciences at MIT. P. J. Tuckman, J. Marshall, and N. Lutsko are supported by NSF Grant OCE-2023520. J. Smyth was supported by the NSF atmospheric and geospace sciences postdoctoral research fellowship (Award 2123372). We thank Jean-Michel Campin and Jeffrey Scott for their technical and modeling contributions to this work.

Data availability statement. The reanalysis data used in this study can be accessed at the climate data store, at

https://cds.climate.copernicus.eu/cdsapp#!/dataset/derived-reanalysis-energy-moisture-budget?tab=form for the divergence of atmospheric energy fluxes and https://cds.climate.copernicus.eu/cdsapp#!/dataset/reanalysis-era5-single-levels-monthly-means?tab=form for all other quantities. A simulation similar to the dynamic ocean simulation used here is available at https://github.com/MITgcm/verification_other/tree/master/cpl_gray\%2Bswamp\%2Bocn. For access to the simulation data or other code, feel free to contact the corresponding author.

APPENDIX

An Idealized Model of the Monsoonal Mode: Formulation and Simple Solution

a. Column-integrated energy budget

Here, we present a derivation of the simplified model of the monsoonal mode used in section 4. We begin with statements of conservation of energy for each column of the atmosphere and the slab ocean:

$$\frac{\partial}{\partial t}\text{atmospheric energy} + \text{advection} = \text{surface flux} - \text{atmosphere OLR}, \quad \text{(A1)}$$

$$\frac{\partial}{\partial t}\text{ocean energy} = -\text{surface flux} - \text{ocean OLR} + \text{solar radiation}, \quad \text{(A2)}$$

where OLR is outgoing longwave radiation.

We now examine each of these terms separately, denoting the mean quantity with an overbar (e.g., $\overline{T}$) and the anomaly with a prime (e.g., T'). All mean quantities are that of a zonally symmetric aquaplanet, and anomalies are with respect to that state. Additionally, we are considering a system at a single latitude, ignoring any meridional structure. The moist static energy of the atmosphere, integrated over a vertical column from the surface to the top of the atmosphere, is given by

$$E_{\text{atm}} = \frac{1}{g}\int_0^{p_s}(c_p T + Lq + gz)dp, \quad \text{(A3)}$$

where all symbols are defined the same way as in section 4. We now separate it into mean and anomaly components noting that Eq. (A3) has three energy terms that may have anomalies: T', q', and z'. We simplify by linearizing with respect to T, assuming that $z' \approx dz/dT|_{\overline{T}}T'$, $q' = \text{RH}q'^{*} \approx \text{RH}dq^{*}/dT|_{\overline{T}}T'$ where $q^{*}(T)$ is the saturation specific humidity and relative humidity (RH) will be assumed to be constant. This allows us to write the energy anomaly in terms of one temperature T':

$$E'_{\text{atm}} \approx \frac{1}{g}\int_0^{\overline{p}_s}\left(c_p + \text{RH}\frac{dq^{*}}{dT}\Big|_{\overline{T}} + g\frac{dz}{dT}\Big|_{\overline{T}}\right)T'dp.$$

Figure 7 suggests the vertical structure of the energy anomaly does not depend on longitude. We therefore assume a separable form for temperature $T' = P(p)T'(x)$, where P is a unitless vertical structure which will be chosen so that $T'(x)$ represents the near-surface atmospheric temperature. It is useful to use the near-surface temperature as it is this temperature that controls surface fluxes. We can now write

$$E'_{\text{atm}} \approx C_A T'(x), \quad \text{(A4)}$$

where

$$C_A \equiv \frac{1}{g}\int_0^{\overline{p}_s}\left(c_p + \text{RH}\frac{dq^{*}}{dT}\Big|_{\overline{T}} + g\frac{dz}{dT}\Big|_{\overline{T}}\right)P(p)dp$$

is the heat capacity (per square meter) of an atmospheric column.

Although several assumptions have been made to obtain Eq. (A4), our slab ocean simulations provide some support. Specifically, in the simulated monsoonal mode, the lowest-level model temperature and the atmospheric energy averaged between the surface and 100 hPa are highly correlated. The slope of a best-fit line through a scatter of these two quantities yields a numerical estimate of the heat capacity C_A of 2.4×10^7 J m^{-2} K^{-1}. This is roughly the heat capacity of a 6-m slab ocean, in accord with the findings of Cronin and Emanuel (2013) for a warm, moist atmosphere.

b. Representation of advection

We now consider the advection term in the atmospheric energy budget equation. We wish to capture two separate effects: 1) low-level zonal wind carrying warm air to the east and 2) upper-level winds spreading energy outward from the location of maximum energy. The first of these can be seen in Fig. 6 bringing warm air to the east. The second is suggested by the presence of strong upward motion at the location of energy maximum in Fig. 7. This must be balanced by upper-level divergence moving from high energy to low energy, approximated here as a mixing/diffusive process. We parameterize these effects as

$$\text{advection} = C_A\left(U_{\text{BL}}\frac{\partial}{\partial x} - \kappa_{\text{FT}}\frac{\partial^2}{\partial x^2}\right)T',$$

where U_{BL} is the boundary layer zonal velocity in the atmosphere and κ_{FT} is an effective diffusivity for the free troposphere.

c. Turbulent fluxes

The major contributions to air–sea fluxes are

$$\begin{aligned}\text{surface flux} &= \text{evaporation} + \text{sensible heating}\\ &= C_{\text{evap}}|\overline{U}|[q^{*}(\text{SST}') - q'] + C_{\text{sens}}|\overline{U}|(\text{SST}' - T'),\end{aligned}$$

where SST′ is the sea surface temperature (SST) anomaly, $q^{*}(\text{SST}') \equiv dq^{*}/dT|_{\overline{\text{SST}}}\text{SST}'$ is the anomalous saturation specific humidity, $|\overline{U}|$ is the wind speed, and C_{evap} and C_{sens} are constants. We expand and ignore terms of order $(\text{SST}' - T')^2$:

$$\begin{aligned}\text{surface flux} &= C_{\text{evap}}|\overline{U}|[q^*(\text{SST}') - \text{RH}q^*(T')] + C_{\text{sens}}|\overline{U}|(\text{SST}' - T')\\ &= C_{\text{evap}}|\overline{U}|\{(1 - \text{RH})q^*(\text{SST}') + \text{RH}[q^*(\text{SST}') - q^*(T')]\} + C_{\text{sens}}|\overline{U}|(\text{SST}' - T')\\ &\approx C_{\text{evap}}|\overline{U}|\left[(1 - \text{RH})q^*(\text{SST}') + \text{RH}\frac{dq^*}{dT}\bigg|_{\overline{T}}(\text{SST}' - T')\right] + C_{\text{sens}}|\overline{U}|(\text{SST}' - T').\end{aligned}$$

Note that we have assumed $dq^*/dT|_{\overline{\text{SST}}} \approx dq^*/dT|_{\overline{T}}$. Rearranging and simplifying, we can write

$$\begin{aligned}\text{surface flux} &\approx \left(C_{\text{evap}}|\overline{U}|\frac{dq^*}{dT}\bigg|_{\overline{T}}\text{RH} + C_{\text{sens}}|\overline{U}|\right)(\text{SST}' - T')\\ &\quad + C_{\text{evap}}|\overline{U}|(1 - \text{RH})q^*(\text{SST}')\\ &\approx \frac{C_A}{\tau}(\text{SST}' - T'),\end{aligned}$$

where we have combined all the terms into a relaxation process. By using C_A in this equation, we ensure that the resulting temperature budget equation has the form $(\partial/\partial t)T' = \cdots - (T' - \text{SST}')/\tau$ and so represents a process which relaxes T' back to SST′ on a time scale τ. To arrive at such a simple expression, we have neglected the last term involving $(1 - \text{RH})$, which is justified if $(1 - \text{RH})/\text{RH}$ is small. Relative humidity is typically larger than 0.8 everywhere in the composite, so this is not unreasonable.

d. Longwave fluxes

We linearize the outgoing longwave flux from the atmosphere as $4\sigma\overline{T}^3T'$, where σ is the Stefan–Boltzmann constant. There is also an absorbed longwave radiation term which depends on the detailed chemical composition, humidity, and temperature of the surrounding area. We incorporate all this complexity into one time scale τ_R and assume that $\text{OLR} \approx T'/\tau_R$ in both the atmosphere and the ocean (with the ocean temperature SST′ for the latter). Note that the time scales at which the atmosphere and ocean lose energy due to longwave radiation are almost certainly different, but for simplicity, we treat them as the same here. The radiation term is small (discussed below), so this assumption does not significantly affect our results.

e. Ocean energy budget

The energy stored in a well-mixed layer of water is $\rho_W c_W d\text{SST}$, where ρ_W is the density, c_W is the specific heat, and d is the depth of the layer. Therefore, the slab ocean heat capacity is $C_O \equiv \rho_W c_W d$, giving an anomalous ocean energy of $C_O\text{SST}'$. This heat capacity has a value of 1.2×10^8 J m^{-2} K^{-1} for a 30-m slab ocean and 8.3×10^6 J m^{-2} K^{-1} for a 2-m slab ocean (i.e., the continent in our simulations). The relevant terms for the ocean energy budget are surface fluxes and outgoing longwave radiation. Incoming solar radiation is ignored as we wish to study the monsoonal mode once it is moving and decaying, and advection is ignored since we are representing a slab ocean. This gives an ocean energy budget equation of

$$\frac{\partial}{\partial t}\text{SST}' = -\frac{C_A}{C_O}\frac{\text{SST}' - T'}{\tau} - \frac{\text{SST}'}{\tau_R}.$$

f. Complete coupled model

In summary, bringing all the equations together, rearranging slightly, and dropping primes, we have

$$\frac{\partial}{\partial t}T + U_{\text{BL}}\frac{\partial}{\partial x}T = \frac{\text{SST} - T}{\tau} - \frac{T}{\tau_R} + \kappa_{\text{FT}}\frac{\partial^2}{\partial x^2}T, \tag{A5}$$

$$\frac{\partial}{\partial t}\text{SST} = -\frac{C_A}{C_O}\frac{\text{SST} - T}{\tau} - \frac{\text{SST}}{\tau_R}, \tag{A6}$$

TABLE A1. Estimates of key parameters associated with the monsoonal mode.

Quantity	Description	Estimated value
U_{BL}	Boundary layer velocity	3 m s^{-1}
k	Wavenumber of mode	2×10^{-7} m^{-1}
T	Boundary layer temperature	0.83 K
$\text{SST} - T$	Air–sea temperature difference	0.31 K
OLR	Longwave flux	4.1 W m^{-2}
Mixing	Equivalent atmosphere mixing flux	29.2 W m^{-2}
Surface flux	Evaporation + sensible flux	24.7 W m^{-2}
τ_R	Radiative time scale	56 days
$\tau_{\text{FT}} \equiv 1/(k^2\kappa_{\text{FT}})$	Mixing time scale	8 days
τ	Surface flux time scale	3 days
$\tau_{\text{AD}} \equiv 1/(U_{\text{BL}}k)$	Advective time scale	19 days

TABLE A2. Key nondimensional numbers and their estimated values.

Name	Dimensional variable	Nondimensional variable	Typical value
Radiative term	τ_R	$\mathrm{Ra} \equiv 1/(U_{\mathrm{BL}} k \tau_R)$	0.34
Free troposphere mixing term	τ_{FT}	$\mathrm{FT} \equiv 1/(U_{\mathrm{BL}} k \tau_{\mathrm{FT}})$	2.4
Surface flux term	τ	$\mathrm{SF} \equiv 1/(U_{\mathrm{BL}} k \tau)$	6.3

which are Eqs. (3) and (4) of section 4. Note that SST and T are anomalies, while U_{BL} is not.

g. Plane wave solutions

We assume that SST and T are plane waves propagating in x and time t:

$$(T, \mathrm{SST}) = (\tilde{T}, \widetilde{\mathrm{SST}})\exp[i(kx - \omega t)],$$

where $\tilde{T}_0$ and $\widetilde{\mathrm{SST}}_0$ are measures of amplitude. Substituting into Eqs. (A5) and (A6), we obtain the following algebraic system:

$$-i\omega\tilde{T} + iU_{\mathrm{BL}}k\tilde{T} = \frac{\widetilde{\mathrm{SST}} - \tilde{T}}{\tau} - \frac{\tilde{T}}{\tau_R} - k^2\kappa_{\mathrm{FT}}\tilde{T}$$

$$-i\omega\widetilde{\mathrm{SST}} = -\frac{C_A}{C_O}\frac{\widetilde{\mathrm{SST}} - \tilde{T}}{\tau} - \frac{\widetilde{\mathrm{SST}}}{\tau_R}.$$

This must have a valid solution for all values of initial conditions, so we define a matrix and set its determinant to zero:

$$\begin{bmatrix} -i\omega + iU_{\mathrm{BL}}k + \dfrac{1}{\tau} + \dfrac{1}{\tau_R} + k^2\kappa_{\mathrm{FT}} & -\dfrac{1}{\tau} \\ -\dfrac{C_A}{C_O\tau} & -i\omega + \dfrac{C_A}{C_O\tau} + \dfrac{1}{\tau_R} \end{bmatrix} \begin{bmatrix} \tilde{T} \\ \widetilde{SST} \end{bmatrix} = 0$$

$$\left(-i\omega + iU_{\mathrm{BL}}k + \frac{1}{\tau} + \frac{1}{\tau_R} + k^2\kappa_{\mathrm{FT}}\right)\left(-i\omega + \frac{C_A}{C_O\tau} + \frac{1}{\tau_R}\right) - \frac{C_A}{C_O\tau^2} = 0$$

To simplify this system, we now estimate typical magnitudes of the various terms, identify key nondimensional numbers–(see Tables A1 and A2) and then neglect small terms. This enables us to arrive at the simple analytical solution that was used in section 4.

In Table A1, the boundary layer velocity is estimated as the maximum value of the eastward wind at the center of the monsoonal mode in the composite below 850 hPa, and the wavenumber of the monsoonal mode is calculated by assuming that the width of the continent is half a wavelength. The T, SST $-$ T, and the energy flux estimates are based on model outputs spanning the equator to 8°N averaged over all months. This allows the energy transport time scales [τ, τ_R, and $\tau_{\mathrm{FT}} \equiv 1/(k^2\kappa_{\mathrm{FT}})$] to be calculated as the ratio of the relevant temperature scale (SST $-$ T or T) to energy flux (divided by the atmospheric heat capacity C_A), based on Eq. (A5). We also estimate an uncertainty for what turns out to be the key time scale (τ_{FT}), by calculating it for each month and at each latitude within the relevant band (0°–8°N), thus obtaining a distribution. This is used to infer the 80% confidence interval shown in Fig. 8. The advective time scale, to which other time scales are compared and is a measure of how long it takes for the monsoonal mode to move one wavelength, is defined and calculated as $\tau_{\mathrm{AD}} \equiv 1/(U_{\mathrm{BL}}k)$.

In Table A2, we define and estimate three nondimensional numbers by comparing the time scales of radiative, mixing, and surface fluxes to the advective time scale. A nondimensional number larger than one means that the term in question acts faster than the advective time scale and is therefore important. We see that the surface flux term is the largest by around a factor of 2–3, followed by the free troposphere mixing term.

The equation for ω can be written in terms of these nondimensional numbers [multiplying both sides by $1/(U_{\mathrm{BL}}k)^2$]:

$$\left(-i\frac{\omega}{U_{\mathrm{BL}}k} + i + \mathrm{SF} + \mathrm{Ra} + \mathrm{FT}\right)\left(-i\frac{\omega}{U_{\mathrm{BL}}k} + \mathrm{SF}\frac{C_A}{C_O} + \mathrm{Ra}\right) - \frac{C_A}{C_O}\mathrm{SF}^2 = 0.$$

As SF is large, we consider the limit that SF $\to \infty$ and separate out equations for different powers of SF:

$$\mathrm{SF}^2 : \mathrm{SF} \times \mathrm{SF}\frac{C_A}{C_O} - \frac{C_A}{C_O}\mathrm{SF}^2 = 0$$

$$\mathrm{SF} : -i\frac{\omega}{U_{\mathrm{BL}}k} + \mathrm{Ra} - i\frac{\omega}{U_{\mathrm{BL}}k}\frac{C_A}{C_O} + i\frac{C_A}{C_O} + \mathrm{Ra}\frac{C_A}{C_O} + \mathrm{FT}\frac{C_A}{C_O} = 0.$$

Solving the linear-in-SF equation for ω/k, we have

$$\frac{\omega}{U_{\mathrm{BL}}k} = -i\mathrm{Ra} + \frac{C_A}{C_A + C_O} - i\mathrm{FT}\frac{C_A}{C_A + C_O}.$$

We now redimensionalize and rearrange to yield our final expression [Eq. (5) of section 4]:

$$\frac{\omega}{k} \approx U_{\mathrm{BL}} \frac{C_A}{C_A + C_O} - \frac{i}{k}\left(\frac{1}{\tau_R} + \frac{1}{\tau_{\mathrm{FT}}} \frac{C_A}{C_A + C_O}\right). \tag{A7}$$

REFERENCES

Abe, M., M. Hori, T. Yasunari, and A. Kitoh, 2013: Effects of the Tibetan Plateau on the onsetof the summer monsoon in South Asia: The role of the air-sea interaction. *J. Geophys. Res. Atmos.*, **118**, 1760–1776, https://doi.org/10.1002/jgrd.50210.

Adam, O., T. Bischoff, and T. Schneider, 2016a: Seasonal and interannual variations of the energy flux equator and ITCZ. Part I: Zonally averaged ITCZ position. *J. Climate*, **29**, 3219–3230, https://doi.org/10.1175/JCLI-D-15-0512.1.

——, ——, and ——, 2016b: Seasonal and interannual variations of the energy flux equator and ITCZ. Part II: Zonally varying shifts of the ITCZ. *J. Climate*, **29**, 7281–7293, https://doi.org/10.1175/JCLI-D-15-0710.1.

Adames, Á. F., and E. D. Maloney, 2021: Moisture mode theory's contribution to advances in our understanding of the Madden-Julian Oscillation and other tropical disturbances. *Curr. Climate Change Rep.*, **7**, 72–85, https://doi.org/10.1007/s40641-021-00172-4.

Adcroft, A., J.-M. Campin, C. Hill, and J. Marshall, 2004: Implementation of an atmosphere–ocean general circulation model on the expanded spherical cube. *Mon. Wea. Rev.*, **132**, 2845–2863, https://doi.org/10.1175/MWR2823.1.

Ahmed, F., and J. D. Neelin, 2019: Explaining scales and statistics of tropical precipitation clusters with a stochastic model. *J. Atmos. Sci.*, **76**, 3063–3087, https://doi.org/10.1175/JAS-D-18-0368.1.

Atwood, A. R., A. Donohoe, D. S. Battisti, X. Liu, and F. S. R. Pausata, 2020: Robust longitudinally variable responses of the ITCZ to a myriad of climate forcings. *Geophys. Res. Lett.*, **47**, e2020GL088833, https://doi.org/10.1029/2020GL088833.

Baldwin, J. W., G. A. Vecchi, and S. Bordoni, 2019: The direct and ocean-mediated influence of Asian orography on tropical precipitation and cyclones. *Climate Dyn.*, **53**, 805–824, https://doi.org/10.1007/s00382-019-04615-5.

Bergemann, M., and C. Jakob, 2016: How important is tropospheric humidity for coastal rainfall in the tropics? *Geophys. Res. Lett.*, **43**, 5860–5868, https://doi.org/10.1002/2016GL069255.

Biasutti, M., and Coauthors, 2018: Global energetics and local physics as drivers of past, present and future monsoons. *Nat. Geosci.*, **11**, 392–400, https://doi.org/10.1038/s41561-018-0137-1.

Bischoff, T., and T. Schneider, 2016: The equatorial energy balance, ITCZ position, and double-ITCZ bifurcations. *J. Climate*, **29**, 2997–3013, https://doi.org/10.1175/JCLI-D-15-0328.1.

Bjerknes, J., 1969: Atmospheric teleconnections from the equatorial Pacific. *Mon. Wea. Rev.*, **97**, 163–172, https://doi.org/10.1175/1520-0493(1969)097<0163:ATFTEP>2.3.CO;2.

Boos, W. R., and Z. Kuang, 2010: Dominant control of the South Asian monsoon by orographic insulation versus plateau heating. *Nature*, **463**, 218–222, https://doi.org/10.1038/nature08707.

——, and R. L. Korty, 2016: Regional energy budget control of the intertropical convergence zone and application to mid-Holocene rainfall. *Nat. Geosci.*, **9**, 892–897, https://doi.org/10.1038/ngeo2833.

Broccoli, A. J., K. A. Dahl, and R. J. Stouffer, 2006: Response of the ITCZ to Northern Hemisphere cooling. *Geophys. Res. Lett.*, **33**, L01702, https://doi.org/10.1029/2005GL024546.

Byrne, M. P., and P. A. O'Gorman, 2013: Land–ocean warming contrast over a wide range of climates: Convective quasi-equilibrium theory and idealized simulations. *J. Climate*, **26**, 4000–4016, https://doi.org/10.1175/JCLI-D-12-00262.1.

——, and T. Schneider, 2016: Energetic constraints on the width of the intertropical convergence zone. *J. Climate*, **29**, 4709–4721, https://doi.org/10.1175/JCLI-D-15-0767.1.

Chang, C.-P., Z. Wang, J. McBride, and C.-H. Liu, 2005: Annual cycle of Southeast Asia—Maritime Continent rainfall and the asymmetric monsoon transition. *J. Climate*, **18**, 287–301, https://doi.org/10.1175/JCLI-3257.1.

Chou, C., J. D. Neelin, and H. Su, 2001: Ocean-atmosphere-land feedbacks in an idealized monsoon. *Quart. J. Roy. Meteor. Soc.*, **127**, 1869–1891, https://doi.org/10.1002/qj.49712757602.

Craig, G. C., and J. M. Mack, 2013: A coarsening model for self-organization of tropical convection. *J. Geophys. Res. Atmos.*, **118**, 8761–8769, https://doi.org/10.1002/jgrd.50674.

Cronin, T. W., and K. A. Emanuel, 2013: The climate time scale in the approach to radiative-convective equilibrium. *J. Adv. Model. Earth Syst.*, **5**, 843–849, https://doi.org/10.1002/jame.20049.

Donohoe, A., J. Marshall, D. Ferreira, and D. Mcgee, 2013: The relationship between ITCZ location and cross-equatorial atmospheric heat transport: From the seasonal cycle to the last glacial maximum. *J. Climate*, **26**, 3597–3618, https://doi.org/10.1175/JCLI-D-12-00467.1.

——, D. M. W. Frierson, and D. S. Battisti, 2014: The effect of ocean mixed layer depth on climate in slab ocean aquaplanet experiments. *Climate Dyn.*, **43**, 1041–1055, https://doi.org/10.1007/s00382-013-1843-4.

——, A. R. Atwood, and M. P. Byrne, 2019: Controls on the width of tropical precipitation and its contraction under global warming. *Geophys. Res. Lett.*, **46**, 9958–9967, https://doi.org/10.1029/2019GL082969.

——, ——, and D. S. Battisti, 2022: Optimal geometric characterization of forced zonal mean tropical precipitation changes. *Climate Dyn.*, **59**, 2181–2196, https://doi.org/10.1007/s00382-022-06203-6.

Frierson, D. M. W., I. M. Held, and P. Zurita-Gotor, 2007: A gray-radiation aquaplanet moist GCM. Part II: Energy transports in altered climates. *J. Atmos. Sci.*, **64**, 1680–1693, https://doi.org/10.1175/JAS3913.1.

Geen, R., F. H. Lambert, and G. K. Vallis, 2019: Processes and timescales in onset and withdrawal of "aquaplanet monsoons". *J. Atmos. Sci.*, **76**, 2357–2373, https://doi.org/10.1175/JAS-D-18-0214.1.

Green, B., and J. Marshall, 2017: Coupling of trade winds with ocean circulation damps ITCZ shifts. *J. Climate*, **30**, 4395–4411, https://doi.org/10.1175/JCLI-D-16-0818.1.

——, ——, and A. Donohoe, 2017: Twentieth century correlations between extratropical SST variability and ITCZ shifts. *Geophys. Res. Lett.*, **44**, 9039–9047, https://doi.org/10.1002/2017GL075044.

——, ——, and J.-M. Campin, 2019: The 'sticky' ITCZ: Ocean-moderated ITCZ shifts. *Climate Dyn.*, **53** (1), 1–19, https://doi.org/10.1007/s00382-019-04623-5.

Harrop, B. E., J. Lu, and L. R. Leung, 2019: Sub-cloud moist entropy curvature as a predictor for changes in the seasonal

cycle of tropical precipitation. *Climate Dyn.*, **53**, 3463–3479, https://doi.org/10.1007/s00382-019-04715-2.

Heddinghaus, T. R., and A. F. Krueger, 1981: Annual and interannual variations in outgoing longwave radiation over the tropics. *Mon. Wea. Rev.*, **109**, 1208–1218, https://doi.org/10.1175/1520-0493(1981)109<1208:AAIVIO>2.0.CO;2.

Hersbach, H., and Coauthors, 2020: The ERA5 global reanalysis. *Quart. J. Roy. Meteor. Soc.*, **146**, 1999–2049, https://doi.org/10.1002/qj.3803.

Hottovy, S., and S. N. Stechmann, 2015: A spatiotemporal stochastic model for tropical precipitation and water vapor dynamics. *J. Atmos. Sci.*, **72**, 4721–4738, https://doi.org/10.1175/JAS-D-15-0119.1.

Kang, S. M., I. M. Held, D. M. W. Frierson, and M. Zhao, 2008: The response of the ITCZ to extratropical thermal forcing: Idealized slab-ocean experiments with a GCM. *J. Climate*, **21**, 3521–3532, https://doi.org/10.1175/2007JCLI2146.1.

Luongo, M. T., S.-P. Xie, and I. Eisenman, 2022: Buoyancy forcing dominates the cross-equatorial ocean heat transport response to Northern Hemisphere extratropical cooling. *J. Climate*, **35**, 6671–6690, https://doi.org/10.1175/JCLI-D-21-0950.1.

Lutsko, N. J., J. Marshall, and B. Green, 2019: Modulation of monsoon circulations by cross-equatorial ocean heat transport. *J. Climate*, **32**, 3471–3485, https://doi.org/10.1175/JCLI-D-18-0623.1.

Ma, D., A. H. Sobel, Z. Kuang, M. S. Singh, and J. Nie, 2019: A moist entropy budget view of the South Asian summer monsoon onset. *Geophys. Res. Lett.*, **46**, 4476–4484, https://doi.org/10.1029/2019GL082089.

Mamalakis, A., and Coauthors, 2021: Zonally contrasting shifts of the tropical rain belt in response to climate change. *Nat. Climate Change*, **11**, 143–151, https://doi.org/10.1038/s41558-020-00963-x.

Marshall, J., A. Adcroft, C. Hill, L. Perelman, and C. Heisey, 1997: A finite-volume, incompressible Navier Stokes model for studies of the ocean on parallel computers. *J. Geophys. Res.*, **102**, 5753–5766, https://doi.org/10.1029/96JC02775.

Mayer, J., M. Mayer, and L. Haimberger, 2022: Mass-consistent atmospheric energy and moisture budget data from 1979 to present derived from ERA5 reanalysis, v1.0. Copernicus Climate Change Service (C3S) Climate Data Store (CDS), accessed 19 May 2022, https://doi.org/10.24381/cds.c2451f6b.

Meehl, G. A., 1987: The annual cycle and interannual variability in the tropical Pacific and Indian Ocean regions. *Mon. Wea. Rev.*, **115**, 27–50, https://doi.org/10.1175/1520-0493(1987)115<0027:TACAIV>2.0.CO;2.

——, 1993: A coupled air-sea biennial mechanism in the tropical Indian and Pacific regions: Role of the ocean. *J. Climate*, **6**, 31–41, https://doi.org/10.1175/1520-0442(1993)006<0031:ACASBM>2.0.CO;2.

Neelin, J. D., and I. M. Held, 1987: Modeling tropical convergence based on the moist static energy budget. *Mon. Wea. Rev.*, **115**, 3–12, https://doi.org/10.1175/1520-0493(1987)115<0003:MTCBOT>2.0.CO;2.

Popp, M., N. J. Lutsko, and S. Bony, 2020: Weaker links between zonal convective clustering and ITCZ width in climate models than in observations. *Geophys. Res. Lett.*, **47**, e2020GL090479, https://doi.org/10.1029/2020GL090479.

Privé, N. C., and R. A. Plumb, 2007a: Monsoon dynamics with interactive forcing. Part I: Axisymmetric studies. *J. Atmos. Sci.*, **64**, 1417–1430, https://doi.org/10.1175/JAS3916.1.

——, and ——, 2007b: Monsoon dynamics with interactive forcing. Part II: Impact of eddies and asymmetric geometries. *J. Atmos. Sci.*, **64**, 1431–1442, https://doi.org/10.1175/JAS3917.1.

Ramesh, N., and W. R. Boos, 2022: The unexpected oceanic peak in energy input to the atmosphere and its consequences for monsoon rainfall. *Geophys. Res. Lett.*, **49**, e2022GL099283, https://doi.org/10.1029/2022GL099283.

Raymond, D. J., and Ž. Fuchs, 2009: Moisture modes and the Madden–Julian Oscillation. *J. Climate*, **22**, 3031–3046, https://doi.org/10.1175/2008JCLI2739.1.

Recchia, L. G., S. D. Griffiths, and D. J. Parker, 2021: Controls on propagation of the Indian monsoon onset in an idealised model. *Quart. J. Roy. Meteor. Soc.*, **147**, 4010–4031, https://doi.org/10.1002/qj.4165.

Schneider, T., T. Bischoff, and G. H. Haug, 2014: Migrations and dynamics of the intertropical convergence zone. *Nature*, **513**, 45–53, https://doi.org/10.1038/nature13636.

Shaw, T. A., A. Voigt, S. M. Kang, and J. Seo, 2015: Response of the intertropical convergence zone to zonally asymmetric subtropical surface forcings. *Geophys. Res. Lett.*, **42**, 9961–9969, https://doi.org/10.1002/2015GL066027.

Sobel, A., and E. Maloney, 2013: Moisture modes and the eastward propagation of the MJO. *J. Atmos. Sci.*, **70**, 187–192, https://doi.org/10.1175/JAS-D-12-0189.1.

Wang, B., LinHo, Y. Zhang, and M.-M. Lu, 2004: Definition of South China Sea monsoon onset and commencement of the East Asia summer monsoon. *J. Climate*, **17**, 699–710, https://doi.org/10.1175/2932.1.

Wang, S., and A. H. Sobel, 2022: A unified moisture mode theory for the Madden–Julian Oscillation and the boreal summer intraseasonal oscillation. *J. Climate*, **35**, 1267–1291, https://doi.org/10.1175/JCLI-D-21-0361.1.

Wei, H.-H., and S. Bordoni, 2018: Energetic constraints on the ITCZ position in idealized simulations with a seasonal cycle. *J. Adv. Model. Earth Syst.*, **10**, 1708–1725, https://doi.org/10.1029/2018MS001313.

Williams, I. N., and C. M. Patricola, 2018: Diversity of ENSO events unified by convective threshold sea surface temperature: A nonlinear ENSO index. *Geophys. Res. Lett.*, **45**, 9236–9244, https://doi.org/10.1029/2018GL079203.

Wu, X., K. A. Reed, C. L. P. Wolfe, G. M. Marques, S. D. Bachman, and F. O. Bryan, 2021: Coupled aqua and ridge planets in the Community Earth System Model. *J. Adv. Model. Earth Syst.*, **13**, e2020MS002418, https://doi.org/10.1029/2020MS002418.

Zhai, J., and W. Boos, 2015: Regime transitions of cross-equatorial Hadley circulations with zonally asymmetric thermal forcings. *J. Atmos. Sci.*, **72**, 3800–3818, https://doi.org/10.1175/JAS-D-15-0025.1.

Zhou, W., and S.-P. Xie, 2018: A hierarchy of idealized monsoons in an intermediate GCM. *J. Climate*, **31**, 9021–9036, https://doi.org/10.1175/JCLI-D-18-0084.1.

Zhou, Z.-Q., R. Zhang, and S.-P. Xie, 2019: Interannual variability of summer surface air temperature over central India: Implications for monsoon onset. *J. Climate*, **32**, 1693–1706, https://doi.org/10.1175/JCLI-D-18-0675.1.